

NOTE TO USERS

This reproduction is the best copy available.

UMI[®]

Using Computer Vision Techniques on CT Scans to Measure Changes in Ventricular Volume to Aid in the Diagnosis of Hydrocephalus

By
Zhengyan Sun

Master of Applied Science (in Computing Science)
Saint Mary's University
April 28, 2005

Copyright [Zhengyan Sun, 2005]



Library and
Archives Canada

Bibliothèque et
Archives Canada

Published Heritage
Branch

Direction du
Patrimoine de l'édition

395 Wellington Street
Ottawa ON K1A 0N4
Canada

395, rue Wellington
Ottawa ON K1A 0N4
Canada

Your file *Votre référence*

ISBN: 0-494-05136-1

Our file *Notre référence*

ISBN: 0-494-05136-1

NOTICE:

The author has granted a non-exclusive license allowing Library and Archives Canada to reproduce, publish, archive, preserve, conserve, communicate to the public by telecommunication or on the Internet, loan, distribute and sell theses worldwide, for commercial or non-commercial purposes, in microform, paper, electronic and/or any other formats.

The author retains copyright ownership and moral rights in this thesis. Neither the thesis nor substantial extracts from it may be printed or otherwise reproduced without the author's permission.

AVIS:

L'auteur a accordé une licence non exclusive permettant à la Bibliothèque et Archives Canada de reproduire, publier, archiver, sauvegarder, conserver, transmettre au public par télécommunication ou par l'Internet, prêter, distribuer et vendre des thèses partout dans le monde, à des fins commerciales ou autres, sur support microforme, papier, électronique et/ou autres formats.

L'auteur conserve la propriété du droit d'auteur et des droits moraux qui protègent cette thèse. Ni la thèse ni des extraits substantiels de celle-ci ne doivent être imprimés ou autrement reproduits sans son autorisation.

In compliance with the Canadian Privacy Act some supporting forms may have been removed from this thesis.

Conformément à la loi canadienne sur la protection de la vie privée, quelques formulaires secondaires ont été enlevés de cette thèse.

While these forms may be included in the document page count, their removal does not represent any loss of content from the thesis.

Bien que ces formulaires aient inclus dans la pagination, il n'y aura aucun contenu manquant.


Canada

Certification

Name: Zhengyan Sun
Degree: Master of Science in Applied Science
Title of Thesis: Using Computer Vision Techniques on CT Scans to Measure Change in Ventricular Volume to Aid in Diagnosis of Hydrocephalus

Examining Committee:

Dr. Kevin Vessey, Dean of Graduate Studies

Dr. David H. S. Richardson, Program Co-ordinator

**Dr. Norman Scrimger, External Examiner
Dalhousie University**

Dr. Norma Linney, Senior Supervisor

Dr. Stavros Konstantinidis, Supervisory Committee

Dr. Shyamala Sivakumar, Supervisory Committee

Dr. Matthias Schmidt, Supervisory Committee

Date Certified: April 21, 2005

@Zhengyan Sun, 2005

ACKNOWLEDGEMENTS

I express my sincere gratitude to all those who helped me to complete this thesis.

First of all, I would like to sincerely thank my supervisor, Dr. Norma Linney, for supervising me. Not only did she provide the research direction, ideas and helpful comments she also had lots of patience and courage.

Secondly, I would like to thank Dr. Schmidt and Jeanette Evans who provided the clinic test data and physical models which made my thesis possible.

Also thanks to my external thesis examiner, Dr. Norman Scrimger and the members of the examining committee, Dr. Konstantinidis and Dr. Sivakumar.

I am grateful to all my friends and professors from Math and Computing Science, Saint Mary's University, for being my surrogate family during the time I stayed there. Special thanks to Dr. Pawan Lingras for giving me the chance to be in this program and to Owen Smith for the technical support. Thank you to the Graduate Studies Office for the scholarship support and to the Natural Sciences and Engineering Research Council for their support.

Finally, I cannot finish this without thanking my parents for supporting me.

Contents

1	Introduction	1
2	Background	4
2.1	Segmentation	4
2.2	Registration	7
2.3	Volume Calculation	10
2.4	Partial Volume Effect	13
2.5	Conclusion	15
3	Theory	16
3.1	Characteristics of CT Images of the Human Head	16
3.1.1	Cerebral Ventricles	17
3.2	Segmentation	18
3.2.1	Segmentation by Thresholding	20
3.2.2	Segmentation by Region Growing	22
3.2.3	Segmentation by Manual Method	23
3.2.4	Canny Edge Detector	24

3.3	Registration	26
3.3.1	Affine Transform: for in-plane movement(2D)	28
3.3.2	Interpolation: for out-of-plane movement(3D)	32
3.4	Partial Volume Effect	33
3.5	Volume Calculation	35
3.6	Measures of Success	36
3.6.1	Similarity Index, S	37
3.6.2	Measures of Success for the Volume Calculation	38
4	Experimental Methods	41
4.1	Clinical Test Data	41
4.2	Segmentation	43
4.2.1	Segmentation by Thresholding	44
4.2.2	Segmentation by Region Growing	44
4.2.3	Segmentation by Manual Method	45
4.2.4	Canny Edge Detection Algorithm	47
4.3	Registration	48
4.3.1	Affine Transform: for in-plane position change	48
4.3.2	Interpolation: for out-of-plane position change	51
4.4	Partial Volume Effect	53
4.5	Volume Calculation	55
4.5.1	Volume Calculation Across Slices (VCAS)	55
4.5.2	Analytical Phantom	56

4.5.3	Physical Phantom	57
4.6	Combination of All Algorithms: CSV	59
5	Experimental Results	61
5.1	Results for Segmentation	61
5.1.1	Thresholding	62
5.1.2	Region growing	63
5.1.3	Thresholding and Region Growing	63
5.1.4	Sensitivity of the Thresholding	64
5.2	Results for Canny Edge Detector	64
5.3	Results for Registration	67
5.3.1	Results for Affine transform (2D)	67
5.3.2	Results for Interpolation (3D)	69
5.4	Results for Volume Calculation	69
5.4.1	Analytical Phantom	69
5.4.2	Physical Phantoms	71
5.4.3	Clinical Double Cases	74
5.4.4	Ratio of Ventricle to Skull	77
6	Conclusion	78
7	Future Work	80
8	Bibliography	81

List of Tables

3.1	Parameters for Analytical Phantom	39
4.1	Parameters for the Canny Edge Detector.	47
5.1	Similarity Index for 15 Clinical Cases	62
5.2	Calculated Volume of Analytical Phantom	70
5.3	Volume of Simple Models	72
5.4	Volume of Simple Models of Water	73
5.5	Volume of Complex Models	73
5.6	Volume of Physical Phantom Taken at 4 Angles	75
5.7	Results of Eight Clinical Double Cases	76
5.8	Ratio of Ventricle to Skull	77

List of Figures

3.1	The Ventricles Viewed From 3 Different Angles	17
3.2	8-Connected Pixels	23
3.3	The Theory of How to Interpolate the Slices	32
3.4	Images with Partial Volume Effect	34
3.5	Bounday Pixels Contain Partial Volume Effect	35
3.6	Analytical Phantom	38
3.7	Physical Phantom Models	40
4.1	Result Images of 3 Segmentation Methods	46
4.2	Process Images of Canny Edge Detector	48
4.3	Result Images after Correlation	50
4.4	Result Image after Rotation	51
4.5	The Interpolation of Out-of-Plane Movement	52
4.6	Partial Volume Effect Correction	55
4.7	Segmented Images for Physical Phantom	58
5.1	Graphs of the Similarity Index for 15 Clinical Cases	65

5.2	Threshold Sensitivity	66
5.3	Results for Canny Edge Detector	66
5.4	Results of Affine Transform	68
5.5	Result after Interpolation	69

List of Symbols

agl : the angle of the head tilt at each time

AT : affine transform matrix

$avg1$: average gray value of region one

$avg2$: average gray value of region two

avg : average gray value of region

A_{ven} : the area of the ventricle

$A1, A2$: the number of pixels in the set segmented using method 1 and 2 respectively

A, B, C : three axes of ellipsoid

α : intermediate angle in calculation

β : intermediate angle in calculation

bc, oe : line

Δv : mean attenuation coefficients of ventricle region

Δs : mean attenuation coefficients of ventricle surroundings

Δvs : mean alternative coefficient of a region which contains ventricle and part of the surroundings

Err : percent error

F : function of registration

$f(x, y)$: an image containing a objects or region of interest

$F(u, v)$: the Fourier transforms of $f(x, y)$

F^* : the complex conjugate of F

$h(x, y)$: a template image contains a region of interest

$H(u, v)$: the Fourier transforms of $h(x, y)$

$H(X | Y)$, $H(Y | X)$: the conditional entropies

$H(X)$, $H(Y)$: marginal entropies

$H(X, Y)$: joint entropy

I_1 : Image taken at time $tm1$

I_2 : Image taken at time $tm2$

I_{tmp} : template image

L_{new} : the new length of the ellipsoid axis in mm after scaling

L_{org} : the original length of the ellipsoid axis

$MI(X, Y)$: mutual information for two variables X and Y

M, N: a image of size M pixels* N pixels

N_p : the number of ventricle pixels

N_{inter} : is the number of slices needed to interpolated

$N_{totalslice}$: total number of slices

oc : the distance between the nose and the large eyeball center

φ : the tilt angle between two images

p : pixel

$P_o(x, y)$: the original image intensity at the position (x,y)

$P_t(x, y)$: the thresholded pixel value at the the position (x,y)

P_s : pixel spacing

R : reference image

R1: radius of small eyeball

R2: radius of large eyeball

s: the translation distance in x direction

s_e : the estimated translation distance in x direction

S: similarity index

S_{avg} : the average similarity index

S_i : the similarity index of slice i

S_{thic} : slice thickness

ST: the sensitive of thresholding

T: threshold

t: the translation distance in y direction

t_e : the estimated translation distance in y direction

T_h : high threshold

T_l : low threshold

T_{new} : new threshold

T_{org} : the original threshold

tm1: time one

tm2: time two

θ : rotation angle

θ_e : the estimated rotation angle

V, V_1, V_2, V_3 : vectors

V_{tot} : total volume of ventricle

V_{el} : volume of ellipsoid

V_i : volume of ventricle in slice i

V_{vs} : volume of a chosen region which contains ventricle and part of surrounding tissue

Using Computer Vision Techniques on CT Scans to Measure Change in Ventricular Volume to Aid in Diagnosis of Hydrocephalus

Zhengyan Sun

Date of submission: March 28, 2005

Abstract

Hydrocephalus causes the size of the cerebral ventricles to change. Current subjective assessment of ventricles by neuroradiologists and neurosurgeons has limited accuracy, because of the complex shape of the ventricular system.

To calculate the volume of the ventricles, an algorithm (CSV) which combined segmentation and volume calculation was developed. The ventricles of a CT scan of the head were segmented and their volumes were calculated. The segmentation method was tested on 15 clinical cases and the similarity index was above 0.7. The volume calculation algorithm was tested on both analytical and physical phantoms. The accuracy of the volume was controlled within an error of 5%. Finally CSV was tested on 8 more clinical cases where the patient had been imaged on two occasions and the outcome diagnosis was known. A volume change of less than 5% in the normal cases and greater than 20% in the cases diagnosed with hydrocephalus was calculated. This shows our algorithm (CSV) is capable of distinguishing hydrocephalus.

Chapter 1

Introduction

Hydrocephalus literally means “water head” or “water on the brain”. It is best defined as an excessive accumulation of cerebrospinal fluid (CSF) within the brain and cranial cavity [36]. In almost every instance, underabsorption of CSF, which is brought on by obstruction of the venous return, seems to be the cause of hydrocephalus. An obstruction of the CSF pathway is the true cause of hydrocephalus since it causes the whole ventricular system to be dilated. Hydrocephalus may be present at birth or develop in early infancy, but usually appears in childhood. Hydrocephalus in childhood has a significant mortality rate. The clinical approach to hydrocephalus is early identification and treatment thus minimizing the disability which is attributed to the distension of the CFS spaces.

Hydrocephalus causes the shape and size of the cerebral ventricles to change. Accurate assessment of the volume of cerebral ventricles on computed tomographic (CT) images of the brain is an important and as yet unsolved problem in neuroradiology.

Subtle changes in ventricular volume occur early in the development or progression of the disease. Current subjective assessment of ventricles by neuroradiologists and neurosurgeons has limited accuracy, because of the complex shape of the ventricular system. Differences in the angulation of slices from one study to the next, also makes direct visual comparison of serial imaging studies difficult. Our research is focused on calculating the volume of the ventricles. The goal of this thesis was to develop a computer vision tool to aid the doctor in the diagnosis of hydrocephalus. This thesis investigates the use of computer vision techniques to calculate and compare the volume of the ventricles from a complete set of CT scan slices taken at two different times.

There are two main phases in this thesis: segmentation and volume calculation. Segmentation methods were applied to extract the ventricle from the CT image of the head. Volume calculation methods were used to calculate the volume of the ventricles once they were segmented from the whole set of data.

Many segmentation methods were investigated and an appropriate method was selected for the application. Based on the characteristics of the CT images, thresholding and region growing methods were chosen. Since sometimes the two sets of data taken at two different times are slightly different because of a small change in the position of the patient's head, registration was necessary before segmentation. In order to increase the accuracy of the segmentation methods, methods to reduce the partial volume effect were implemented. To verify the segmentation algorithms, 15 sets of clinical CT scan images were tested and the similarity index was calculated

to be above 0.7. The volume calculation algorithm (CSV) was tested on an analytical phantom and created physical phantoms and the accuracy of the volume was controlled within an error of 5%. Finally CSV was tested on 8 more clinical cases where the patient had been imaged on two occasions and the outcome diagnosis was known. CSV showed a volume change of less than 5% in the normal cases and greater than 20% in the cases diagnosed with hydrocephalus. This shows that our algorithm (CSV) is capable of distinguishing between the normal and diseased cases that were tested.

This thesis is organized as follows. In chapter 2, the existing literature on segmentation, partial volume effects, registration and volume calculation algorithms is surveyed. In chapter 3, the background theory of our algorithms is provided. Chapter 4 describes the detailed methods used in these algorithms. Chapter 5 presents the results when the algorithms were tested on analytical phantoms, physical phantoms and clinical data. Chapter 6 gives our conclusions and Chapter 7 contains the suggestions for future work.

Chapter 2

Background

As our method of calculating the volume of the ventricles involves segmentation, registration, partial volume effect and volume calculation, the current literature on these techniques is first reviewed.

Since the application of these techniques to the calculation of the volume of the ventricles to aid in the diagnosis of hydrocephalus is novel, none of the papers reviewed directly cover this topic. These papers give an indication of the current research on the component techniques.

2.1 Segmentation

Image segmentation is the partitioning of an image into meaningful regions based on some characteristic, such as the properties of the pixels. Image segmentation techniques can be classified as surface-based approaches, where the surface of an object is approximated using a stack of 2-D contours, or volume-based approaches

where objects are represented as continuous 3-D volume. In the 3D approach, 2-D slices are stacked together and the missing data between the slices are usually estimated by interpolation. Then the 3D object of interest is isolated.

Image segmentation techniques can also be classified either as a statistical approach or structural approach. The statistical approach generates the probability distribution function of the image pixels or generates the parameters to characterize the properties of the tone and texture [1]. A structural approach might analyze the tone and texture in terms of their organization and relationship [2]. Region growing [18], wavelet transforms [18], [42], Markov random fields (MRF) [10][17][28] and Gaussian random fields (GRF) [14][23][43] are all examples of segmentation techniques which use a structural approach.

Since there are many types of segmentation methods, selecting a method suitable for our application was the first challenge. Liew and Yan [29] discuss the trade off between 2D and 3D segmentation. The authors presented an adaptive spatial fuzzy clustering segmentation algorithm which can suppress the non-uniformity artifact in 3-D MR images. The algorithm applies a dissimilarity index that considers the effect of neighboring pixels. If the neighborhood window is in a non-homogeneous region, the influence of the neighboring pixels on the center pixel is suppressed; otherwise, the center pixel is smoothed by its neighboring pixels during cluster centroid computation. The authors also included quantitative evaluation of the performance of the algorithm. They compute the misclassification rate (MCR) for the segmentation. The MCR is defined as the number of pixels misclassified by the algorithm divided by the total

number of pixels in the image.

The easiest segmentation method to apply is thresholding. Thresholding involves segmenting out the region of interest by selecting an appropriate gray level as a threshold. Kostis et al. [26] described 3-D methods for volumetric doubling-time estimation in small pulmonary nodules of high-resolution CT images. Their method was initially based on mean and gradient-based thresholding techniques. Various measures were used to evaluate and improve the accuracy of nodule segmentation. The 3-D segmentation methods in their paper are model-based and implemented with techniques from mathematical morphology. The segmentation methods they used were global thresholding and morphological opening. Global thresholding methods use a threshold which is determined from the whole image. Global thresholding was found not to be sensitive enough for our application. Local thresholding, based on a region of interest, was found to be more applicable.

Before applying any segmentation method, it is useful to identify a region of interest. This allows the segmentation method to be selected based on the characteristics of a smaller region of the image rather than the entire image. In [3], Ashburner and Friston mentioned a way to identify the region of interest. Their method used voxel-based morphometry involving a voxel by voxel comparison of the gray matter from two groups of subjects. The main idea of this method is to normalize the images, segment the gray matter from the normalized image, and then smooth the segmented images. Voxel-wise parametric statistical tests are used to compare the smoothed images from the two groups. The images are first registered onto the same template

image by affine transformation. Then the normalized image is partitioned into different classes using a modified mixture of model cluster analysis techniques. Finally the image is smoothed with a Gaussian kernel and a statistical analysis is done to identify the gray matter and segment it out. To identify the region of interest a clustering method is used. However, the clustering method was computationally expensive.

Another popular extraction method is the Hough transform(HT). In Zheng et al. [44], the authors use the Hough transform to solve the repeatability, occlusion and out-of-plane motion problems when extracting vertebrae from x-ray images of the back. They used Fourier descriptors to describe the vertebral body shape within their HT algorithm. From these they can obtain affine transform parameters, such as scale, rotation and center position. The method has been applied to a calibration model and to human lumbar spine motion images. The results show the algorithm works well for object extraction from poor quality images. For some digital videofluoroscopic (DVF) images, their method can achieve satisfactory results, but in some cases it failed. Moreover, the method only considered the vertebrae separately, so that the shape was simple enough to employ a look-up table for the Fourier descriptors. This method was not applicable to our problem as the shape of the ventricles is too complex in three dimensions.

2.2 Registration

Registration is the process of matching features of interest from one image to another. There are several image registration applications: registration of the same subject

with the same modality but at different times, registration of the same subject but different modalities, and registration of scans from different subjects. In this thesis, the registration method will only be applied to images of the same subject with the same modality (CT scan) but at different times. An example would be the CT scan image of the patient's head taken on two different clinic visits.

A number of registration methods have been developed: the thin plate splines algorithm [7], spline transformation [41], the iterative closest point algorithm [39] or the balloons model [12]. Other registration methods require mechanical models, either elastic [6], or fluid [11]. Finally, some registration procedures are voxel-based methods. Collins [13] estimates a locally affine transformation that maximizes the cross correlation of the image gradient. Musse [31] proposes a method based on the minimization of the displaced frame difference.

A very common method used in registration is the affine transform which uses three variables: rotation, scale and translation. Finding these three parameters so that the registration result is optimized is a major problem. Jie and Anand [21] present a new information metric, ρ , for affine and multiple image registration. Given images X and Y, the metric $\rho(X,Y)$ was defined as the sum of the conditional entropies $H(X | Y)$ and $H(Y | X)$. So for two images X and Y, $\rho(X,Y) = H(X | Y) + H(Y | X)$. The definition of mutual information for two variables X and Y is $MI(X,Y) = H(X) + H(Y) - H(X,Y)$, where $H(X)$ and $H(Y)$ are marginal entropies and $H(X,Y)$ is joint entropy. Then they found the relationship between the information metric and mutual information MI, $\rho(X,Y) = H(X,Y) - MI(X,Y)$, where ρ is the nonoverlapping

regions and MI is the common region between the two images. They minimize ρ or maximize MI to recover rotation and scale variables.

Excessive computation time is a major problem in registration algorithms. Rohde et al. [34] worked out a way to reduce the algorithm's running time. They used an approach to identify the mis-registered region and then work on correctly registering only this region to avoid useless computations. Moreover, to make sure that the optimization process that produces the transformations is working properly, they also developed a new, precise method to ensure that the Jacobian matrix of the deformation field remains uniformly invertible. All these approaches together, were called the Adaptive Bases Registration Algorithm – a new nonrigid registration algorithm. They have also implemented a method which is similar to traditional ones in which there is no need to identify the misregistered regions. Results show that the adaptive bases algorithm is about 3.5 times faster than the traditional approach. For each registration, the adaptive bases registration algorithm is at least as accurate as measured by the final value of the cost function, as the traditional approach.

Besides affine registration, correlation transformation is another popular method used to address the registration problem. Hipwell et al. [20] proposed a new method for aligning three-dimensional (3-D) magnetic resonance angiography (MRA) images with 2-D X-ray digital subtraction angiograms (DSA). This method was developed from their previous algorithm to register computed tomography volumes to X-ray images based on intensity matching of digitally reconstructed radiographs (DRRs). To make the DSA and DRR more similar, they carried out some transformations

on the MRA images. The registrations were tested on images of a physical neuro-vascular phantoms and images obtained during four neuro-vascular interventions. They examined performance measures when the algorithm produced DRRs using four different strategies. They concluded that the most accurate and robust registrations were obtained using the pattern intensity, gradient difference, and gradient correlation similarity measures when the algorithm created DRRs from a binary segmentation of the MRA. This is an intermodal registration technique.

Once an algorithm is developed, it must be evaluated using objective measures. Livyatan et al. [30] discussed a way to validate the registration method. The authors used a gradient-based method for rigid registration of a patient's preoperative computed tomography (CT) scan to its intraoperative situation with a few fluoroscopic X-ray images obtained with a tracked C-arm. For validation, they overlay the bone edge contours directly onto the fluoroscopic X-ray images to show how far the bone model is away from the position it should be. This method is not applicable to our application since it is difficult to isolate the edges of the ventricles.

2.3 Volume Calculation

The ultimate goal of this thesis is to calculate the change in the volume of the ventricles. There are a number of ways to do this. One method of doing this is to calculate the volume of the ventricles at different points in time. The volume calculation method which is accomplished after image segmentation is based on the following idea: First, calculate the area of ventricle in each slice, then multiply the area by the

slice thickness. The next three papers use similar theory to calculate the volume, but the methods are different.

Ashtari et al. [4] developed a menu-driven semi-automated computer system to assess in-vivo brain morphometry using a 3-D MRI of the whole brain. The main steps for their algorithm were defined as follows. Find a starting edge point by searching along rays that emanate from a random starting point until a gradient exceeding a threshold is encountered. Then a path along the boundary is traced to search for the next edge point. The process ends when the path returns to the starting edge point or the path length exceeds a predetermined value. The area of the closed boundary is calculated by using a discrete version of Stokes theorem. Finally, the volume of the feature is calculated by multiplying the area of the feature by the slice thickness.

Alternatively, Brassow and Baumann [8] calculate the volume of the ventricle in each slice and then add them up. In order to measure the ventricular volume, they used the numerical prints of the CT on which the margin between brain tissue and ventricles was drawn. The curves of the ventricles were measured by a curve digitizer. A digital computer was used to add the volume of the pixels in the region of interest in spite of the different magnification on the numerical print in the x- and y-axis. The volumes of all slices were added, taking the small amount of overlapping into account. The method can be useful in special cases to determine tumor size in the brain.

The volume calculation method mentioned in the above two papers involved segmentation. Rottenberg et al. [35] developed a volume estimation method (partial volume analysis, PVA) which does not use any segmentation, and compared this method

with two other volume calculation methods which needed segmentation, computerized planimetry and bi-level decomposition. In the computerized planimetry method, the edge of the ventricle was traced on the video screen by cursor, ventricle volume was determined by multiplying the area within each freehand contour by the slice thickness and summing over the total number of slices. In bi-level decomposition, the range of the ventricle pixel values was found. The volume is then equal to the effective voxel volume multiplied by the number of voxels with mean attenuation coefficients which fall within a range. Rottenberg et al. made an assumption in the third method (PVA) that the ventricular contents and the ventricular surroundings are homogeneous substances with mean attenuation coefficients Δv and Δs . The volume V_{vs} of a chosen region of interest which indicates the ventricle and part of the surrounding tissue was assumed to have a mean alternative coefficient of Δvs . The volume of the ventricles, V_i , was calculated by this formula:

$$V_i = V_{vs}(\Delta vs - \Delta s)/(\Delta v - \Delta s) \quad (2.1)$$

The accuracy of the volume was within 3% of the true volume. Computerized planimetry and bi-level decomposition provide similar estimates of ventricle volume since they both involve similarly segmented images. In contrast, PVA provides a more accurate estimate of ventricular volume. However, PVA is a manual method and it appears to be more sensitive than either of the other methods to changes in Δs or Δv .

2.4 Partial Volume Effect

The partial volume effect (PVE) arises in volumetric images when more than one tissue type is represented by a single voxel. In such cases, the voxel intensity depends not only on the imaging sequence and tissue properties, but also on the proportions of each tissue type present in the voxel. If the pixel is not included in the correct region, the shape and size of the region will be affected. Of course, finally, it will affect the total volume. There are various methods to reduce the partial volume effect, some of which are reviewed below.

The partial-volume problem of the CT image was illustrated by Kostis et al. [26] using a quadrant of a unit circle sampled on a regular grid. Pixels were set if 50% of their area corresponded to the interior of the circle. First, the quadrant was contained within a single pixel. Then, to define an appropriate sampling grid, the quadrant was divided, or supersampled, by a power of two. The degree of resampling of the image, or the supersampling ratio, was the number of divisions of the original number of pixels in the X and Y directions. With this model, they also discuss the accuracy of the area measurement of the circular segment. If the degree of subdivision of the sampling grid increased, the error of the circle area estimation decreased.

For virtual screening techniques, segmentation means the removal of unwanted material. The partial volume effect also makes this segmentation problem more complicated, since this effect causes regions of noninterest and non-existing surfaces to show up. Lakare et al. [27] proposed a novel approach for segmentation and digital cleansing of endoscopic organs. This method is fast and accurate. It also decreases

the undesirable partial volume effect, while some other current approaches do not. For segmentation and digital cleaning, they use the peculiar characteristic exhibited by the intersection of any two distinct-intensity regions. To detect these intersections they cast rays through the volume. They call these rays the segmentation rays as they assist in the segmentation. They then do reconstruction and classification with each intersection the ray detects. To improve the quality of the volume rendering, they further use volumetric contrast enhancement to reconstruct the surface lost by segmentation. They concluded that the algorithm was able to remove all the fluid and stool voxels accurately. Also their method was able to detect and remove stool deposits as thin as one voxel thick (about 0.7 mm) and able to unearth all the mucosa voxels lying below the fluid at the intersection of fluid with the colon wall. This algorithm is especially useful when there are partial volume effect concerns. This method identifies the boundary pixels by using the segmentation rays, then groups this kind of pixel into one of the structures (or regions). This is a really good idea, but here another question appears, “Which region did these boundary pixels belong to?” In this paper, the authors just put these pixels into an arbitrary region. This will increase the error.

In the above two methods, the partial volume effects are considered after the image has been reconstructed. In [32], Muzic et al. developed a method that does not need image reconstruction. The method extends Huesman’s method for scatter and spatial resolution effects while keeping the advantages of computational efficiency. Moreover, the method provides an estimate of the variance of the region of interest

(ROI) radioactivity estimate which can be used to define weights in the kinetic data analysis to ensure unbiased parameter estimates. They evaluate the method using simulation and measured data. It shows that with an appropriate scatter and spatial resolution effects model, it is unbiased and has the ability to quantify myocardial concentration with no more than a 5% error. Thus this method is computationally efficient and it provides estimates of ROI variance which are particularly useful in kinetic modeling analyses.

2.5 Conclusion

All of the above is the literature review for the techniques: segmentation, registration, partial volume effect, and volume calculation. These papers give good background for the techniques that were used to develop the volume calculation algorithm (CSV) of this thesis. The purpose of this algorithm (CSV) was to use computer vision to aid in the diagnosis of hydrocephalus.

Chapter 3

Theory

3.1 Characteristics of CT Images of the Human Head

Computerized tomography (CT) scans are a series of cross-sectional X-ray images of the body. The body is X-rayed from many directions and the cross-sectional image is reconstructed by a computer. The computer generates images of cross-sections (slices) of the body using tomographic principles. CT scans show details of the shape and location of soft tissues, as well as bones and blood. The data in the reconstructed CT image is scaled so that it may be represented by image pixel values ranging from 0 (representing black) to 255 (representing white).

The medical images used in this study were obtained from the Izaak Walton Killam (IWK) Health Center and are the images formed from CT scans of the various patients' heads. Since each image is a cross-section of the head at a particular location

Figure 3.1 removed due to copyright restrictions.

Figure pictures can be viewed at:

http://oracle.crump.ucla.edu:8001/pet/pba/figures-2.tcl?illustration_id=356&folder_id=44

http://oracle.crump.ucla.edu:8001/pet/pba/figures-2.tcl?illustration_id=358&folder_id=44

http://oracle.crump.ucla.edu:8001/pet/pba/figures-2.tcl?illustration_id=358&folder_id=44

Figure 3.1: *The ventricles viewed from three different angles [47].*

and the entire series of these images forms a complete head, each image contains a portion of the skull. Some images include cross-sections of the eyeballs or nose and some of them include ears. A number of images in the complete sequence contain cross-sections of the ventricles. Depending on the angle and location of the slice, the shape of these objects varies from slice to slice.

3.1.1 Cerebral Ventricles

The entire surface of the central nervous system is bathed by a clear, colorless fluid called cerebrospinal fluid (CSF). Cerebrospinal fluid is the cushiony fluid that protects the brain and spine from trauma. The CSF is contained within a system of fluid-filled cavities called ventricles. The ventricle has an uneven shape since it is a combination of three parts (Fig. 3.1): the lateral ventricles, the third ventricle, and the fourth ventricle. The lateral ventricles are two curved openings (shaped like a horseshoe) located within the cerebrum, that provide a pathway for cerebrospinal fluid. The two lateral ventricles are the largest of all the ventricles in the brain, and one is on each side of the brain. In addition to the two lateral ventricles, there is the third ventricle and the fourth ventricle. The third ventricle is a narrow, four-sided, irregularly shaped opening between the two hemispheres that provides a pathway for cerebrospinal fluid.

The fourth ventricle is a diamond shaped cavity located behind the pons and medulla oblongata. It forms the central canal of the spinal cord and protects the brain from trauma [46].

The reconstructed images of the skull have a gray scale range from 0-255 with the black background having an average gray value of zero and the white skull having an average gray value of 255. The tissue inside the skull surrounding the ventricle has an average gray value of approximately 120 while the ventricles themselves have gray values averaging approximately 60. Since the shape of the ventricles is complex and variable, segmentation methods which depend on object shape are difficult to implement. The gray level ranges of the background, skull, brain tissue, and ventricles are reasonably distinct thus making thresholding techniques applicable.

3.2 Segmentation

In the analysis of objects in images, it is important to distinguish the objects of interest from the rest of the image. The techniques that are used to find the objects of interest are referred to as segmentation techniques.

Segmentation methods can be divided into three groups. The first is based on global knowledge about an image or its parts. The knowledge is usually represented by a histogram of the gray level of image features. Examples of these methods are thresholding and clustering. The second is edge-based segmentation, using tools such as the Canny edge detector [38]. The third is region-based segmentation, such as Region growing. Many different characteristics, such as brightness and texture, may

be used in edge detection or region growing. Since the various edge and region-based algorithms have different natures, they may give different results and information.

The global knowledge-based segmentation is used to determine which components of a data set naturally belong together by drawing a histogram which depends on the gray-level, color or shapes included in the whole image.

Edge-based segmentation represents a large group of methods based on information about edges in the image. It was one of the earliest segmentation approaches and still remains very important. Edge-based segmentations rely on edges found in an image by edge detecting operators. The image resulting from edge detection cannot be used alone as a segmentation result. Supplementary processing steps must follow to combine edges into edge chains that correspond to the borders in the image. Then a region must be identified inside the edges.

The aim of the edge-based segmentation methods is to find borders between regions. The region-based segmentation methods construct regions directly. It is easy to construct regions from the borders, and also easy to detect the borders of the regions. However, the segmentation results from edge-based methods and region-based methods usually are not exactly the same. Region growing techniques are generally better in noisy images, where borders are extremely difficult to detect. Homogeneity is an important property of regions and is used as the main segmentation criterion in region growing, where the basic idea is to divide an image into zones of maximum homogeneity. The criteria for homogeneity can be based on gray-level, color, texture, shape and/or model [37].

3.2.1 Segmentation by Thresholding

Gray-level thresholding is the simplest segmentation process. Many objects or image regions are characterized by a constant average x-ray absorption level which translates to a distinct average pixel value. From this average value a brightness level or threshold can be determined to segment objects from the background. Thresholding is computationally inexpensive and fast. It is the oldest segmentation method and is widely used in simple applications [37]. Global and local thresholding are two basic ideas of thresholding. Global thresholding takes a threshold which is determined from the whole image. Local thresholding takes a threshold from a region of interest. Global thresholding was not sensitive enough for our application. Local thresholding, based on a region of interest, was found to be more applicable and was used in this thesis. Local thresholding techniques, which make decisions based on local pixel information, are effective when the intensity levels of the objects fall squarely outside the range of levels in the background. The characteristic of the head image described in section 3.1 contains four distinct gray levels: the background color which is zero, the average skull value of approximately 255, the average gray value of the ventricle of approximately 60 and the average gray value of the remaining brain tissue of approximately 120. Thus using the thresholding method is reasonable.

The technique is based upon a simple concept. A parameter, T , called the brightness threshold, is chosen and applied to the images as follows:

$$\textit{if } P_o(x, y) \geq T, \quad P_t(x, y) = 1; \quad \textit{else } P_t(x, y) = 0. \quad (3.1)$$

where $P_o(x, y)$ is the original image intensity at the position (x, y) and $P_t(x, y)$ is the thresholded pixel value at the same position. This version of the algorithm assumes that there are only two different gray level regions and that we are interested in light objects on a dark background.

The principal difficulty with thresholding methods is selecting a threshold that will provide consistent results. If an image contains very distinct gray level regions, the threshold is easy to choose, but if the gray levels of the features are much closer in value, the threshold is more difficult to select. Also if the average gray level of the feature changes from image to image it becomes difficult to select a universal threshold. When the gray levels of the features cannot be separated, thresholding methods always segment out the features which are not of interest. There are various ways to get a threshold. One method is to build a histogram of all the pixel values and find the range of the gray values in the region of interest. Alternatively a patch of the region of interest may be selected and the average gray value of the patch used as the threshold.

Another issue when using thresholding is the sensitivity of the threshold. Since the method must be tested on hundreds of slices, the threshold selected from one slice should also be valid for other slices. If the segmentation technique is too sensitive to the threshold, the results will not be reliable and the method would be impractical. To test the sensitivity of the thresholding method the threshold was increased/decreased for each slice to see if the total number of pixels segmented changed. If the total number of pixels changed at a new threshold, the program stopped and the sensitivity

was calculated.

$$ST = |T_{new} - T_{org}| / T_{org}. \quad (3.2)$$

where ST represents the sensitivity of the thresholding, T_{new} is the new threshold and T_{org} is the original threshold. The larger the calculated sensitivity, the better the thresholding techniques performs.

3.2.2 Segmentation by Region Growing

Region growing is an approach to image segmentation in which neighboring pixels are examined and added to a region class if no edges are detected. This process is iterated for each boundary pixel in the region. If adjacent regions are found, a region-merging algorithm is used in which weak edges are dissolved and strong edges are left in tact. Region growing offers several advantages over conventional segmentation techniques. Unlike gradient and Laplacian methods, the borders of regions found by Region growing are perfectly thin and connected (since the algorithm only adds single pixels to the exterior of a region). The algorithm is also very stable with respect to noise. The region will never contain too much of the background, as long as the parameters are defined correctly. In our algorithm, the parameters are mean and standard deviation (see section 4.2.2). Other techniques that produce connected edges, like boundary tracking, are very unstable [18].

However, there are several disadvantages to region growing. First and foremost, it is very expensive computationally (processing power and memory usage). It also is complex to implement the algorithms efficiently.

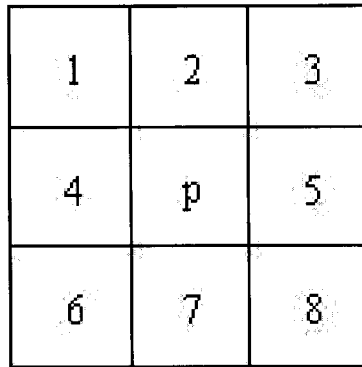


Figure 3.2: Pixel at 1,2,3...8 are 8-connected pixels of pixel p .

The idea of region growing is to start with a pixel (seed) or a set of pixels (seeds) which belongs to the object of interest, and then to iteratively check and decide for each neighboring pixel whether it belongs to the same object or not. Two criteria must be met for a pixel to be annexed to a region: (1) the absolute gray-level difference between any pixel and the seed has to be less than a threshold. (2) the pixel (p) has to be 8-connected (Fig. 3.2) to at least one pixel in that region. Eight connected refers to the following situation. A pixel p at coordinate (x,y) has eight horizontal, vertical and diagonal neighbors whose coordinates are given by $(x+1,y)$, $(x-1,y)$, $(x,y+1)$, $(x,y-1)$, $(x+1,y+1)$, $(x+1,y-1)$, $(x-1,y-1)$, $(x-1,y+1)$. This set of pixels is called the 8-connected pixels of p . The threshold was the average gray value of the region of interest, a patch which was selected by the user manually.

3.2.3 Segmentation by Manual Method

Currently, in order to diagnose a case of hydrocephalus, a radiologist visually evaluates the CT scans of the head and combines the information gained from that with clinical evidence. Thus a manual segmentation technique was taken as the current standard

for the purpose of comparison in this thesis. Therefore, to evaluate the thresholding and region growing methods, a manual segmentation technique was developed to allow comparison of these techniques with the visual evaluation completed by the radiologist.

The manual method has one main drawback. In the manual method, the ventricle edge is highlighted by a radiologist and the edge is extracted. The size of the area outlined by the edge affects the size of the ventricle. How much area the edge will include totally depends on the visual skill of the radiologist. External factors from human vision can affect the results. For example the size of the image, the distance between the radiologist's eyes and the image, and the angle of sight of the radiologist etc., all affect the radiologist's judgements. That is the reason our algorithm (CSV) was developed since CSV segments out the ventricles depending on the pixel value, not subjective judgement. However, to validate our segmentation technique it is valuable to compare the automated techniques to the manual techniques.

3.2.4 Canny Edge Detector

The Canny edge detection operator was developed by John F. Canny in 1986 and uses a multiple stage algorithm to detect a wide range of edges. Most importantly, Canny also produced a computational theory of edge detection explaining why the technique works. Canny's aim was to discover the optimal edge detection algorithm.

The Canny algorithm includes three stages. First, for noise reduction, the raw image is convolved with a gaussian mask. The output appears as a slightly blurred

version of the original. Therefore a single noisy pixel has little effect on the gaussian smoothed image. The second step is to find the intensity gradient of the image and trace the edges through the image. An edge in an image may point in a variety of directions, so the Canny algorithm uses four masks to detect horizontal, vertical and diagonal edges. The results of convolving the original image with each of these masks are stored. For each pixel, the largest result at that pixel is marked, and the direction of the edge determined. From the original image, a map of intensity gradients at each point in the image was created, including the direction of the intensity gradient. Finally, the edges are traced through the image. The higher intensity gradients are more likely to be edges. Since there is not an exact value at which a given intensity gradient switches from not being an edge into being an edge, Canny uses thresholding with hysteresis. Thresholding with hysteresis requires two thresholds - high and low. Making the assumption that important edges should be in continuous lines through the image allows us to follow a faint section of a given line, but avoid identifying a few noisy pixels that do not comprise a line. Therefore the algorithm begins by applying a high threshold. This marks out the edges that are most likely genuine. Starting from these, using the directional information derived earlier, edges can be traced through the image. While tracing a line, the algorithm applies the lower threshold, which allows faint sections of the lines to be included. Once this process is complete, the resulting image is a binary image where each pixel is marked as either an edge pixel or a non-edge pixel.

The Canny algorithm contains a number of adjustable parameters which can affect

the computation time and effectiveness of the algorithm. The first is the size of the gaussian filter. Smaller filters cause less blurring, and allow detection of small, sharp lines. Larger filters cause more blurring, smearing out the value of a given pixel over a larger area of the image. This is more useful for detecting larger, smoother edges. The second is the thresholds. The use of two thresholds allows more flexibility than in a single-threshold approach, but the general problems of thresholding still apply. A threshold set too high can miss important information. A threshold set too low will falsely identify irrelevant information as important. It is difficult to give a generic threshold that works well on all images. No tried and proven approach to this problem yet exists. However, the Canny algorithm is adaptable to various environments. Its parameters allow it to recognize edges of differing characteristics depending on the particular requirements of a given implementation [38].

3.3 Registration

Image registration is a fundamental task in image processing used to match two or more images taken, for example, at different times, from different sensors, or from different viewpoints of the same patient. A good example of the requirement for registration is drawn from in radiotherapy treatment. Here the use of MRI and CT combined would be beneficial, as the former is better suited for delineation of tumour tissue, while the latter is needed for accurate computation of the anatomic structures. Registration is required to map the physical structures from one modality to the other. In the hydrocephalus application examined in this thesis, registration is required to

relate CT images of the same patient taken at different times with slight variations in the point of view.

Registration mappings may be classified as rigid or non-rigid, where rigid mappings are those that preserve all distances. Because of the rigidity of bone and the relative rigidity of anatomy that is attached to bone, and in particular the contents of the skull, rigid mappings are of special importance to this thesis. Rigid mappings may be specified in terms of a translation and a rotation.

Image registration establishes spatial correspondence between a template image I_{tmp} and reference image R . The process of registration establishes which point on template image I_{tmp} corresponds to a particular point on the reference image R . The task of image registration is to find the correspondence function F such that $R = F(I_{tmp})$ without, or at least with minor, human interaction.

There are two kinds of variations in head position: in-plane position change (2D) and out-of-plane, or across the slices, position change (3D). When the same patient has a CT scan taken at two different times, it is possible that the head is not set at exactly the same position in both scans. It might be moved to the right or left a little bit or it might have turned a little for the second scan. These kinds of changes are in-plane, or 2D. If the patient's head position is changed up or down between scans, that causes a 3D position change. When these position changes exist, the CT scans which have been taken at two different times appear different. The volume of the ventricle calculated from these two series of images cannot be accurately compared. Therefore, it is necessary to register the image, I_2 , which was taken at time two, $tm2$,

back to the image, I_1 , which was taken at time one, $tm1$.

Affine transformations are a very common registration method and were used with the 2D position change. For 3D position change an interpolation method was developed to obtain a new slice from previous and later slices. These methods are discussed in detail in the next sections.

3.3.1 Affine Transform: for in-plane movement(2D)

A generic medical image registration scheme may consist of the selection of the image features that will be used during the matching process, the definition of a measure of match (MOM) that quantifies the spatial matching between the reference and the transformed image, and the application of an optimization technique that determines the independent parameters of the transformation model according to MOM. In our method, an affine transform was used to map one image to another. The parameters of the transform were optimized by minimizing the standard deviation of the difference image created from the reference image and the registered image.

The affine transformation can be decomposed into a linear transformation and a simple translation. Assume there are two images I_1 and I_2 , and the intensity value of each pixel in each image has an independent random variable. To register image I_2 to image I_1 , the affine transform is determined as a combination of rotation and

translation. The translation matrix, Tr , is defined as :

$$Tr = \begin{bmatrix} 1 & 0 & s_e \\ 0 & 1 & t_e \\ 0 & 0 & 1 \end{bmatrix} \quad (3.3)$$

where s_e and t_e are the translation distances in x and y directions respectively. The rotation matrix, $R(\theta)$, is defined as:

$$R(\theta) = \begin{bmatrix} \cos(\theta_e) & -\sin(\theta_e) & 0 \\ \sin(\theta_e) & \cos(\theta_e) & 0 \\ 0 & 0 & 1 \end{bmatrix} \quad (3.4)$$

where θ_e is the rotation angle. The combination of the above two matrices is the affine transformation, AT :

$$AT = \begin{bmatrix} \cos(\theta_e) & -\sin(\theta_e) & s_e \\ \sin(\theta_e) & \cos(\theta_e) & t_e \\ 0 & 0 & 1 \end{bmatrix} \quad (3.5)$$

Correlation was used to estimate the translation parameters (s_e and t_e) and edge detection and geometry were used to estimate the angle between edges as the rotation angle (θ_e). The parameters were then optimized by minimizing the standard deviation of the error image over a range of values around the original parameter estimate.

Translation Parameter Estimates (s_e and t_e)

The principal use of correlation is for matching. Let $f(x, y)$ be an image containing an object or region of interest, $h(x, y)$. Usually the object or image region $h(x, y)$ is called a template. If there is a match between the image and the template, the correlation of the two functions will be maximum at the location where h finds a correspondence in f . In our case, the image I_2 was selected as the template image $h(x, y)$ and the image I_1 was used as the $f(x, y)$. Then the correlation method was used to find the translation parameters. The details of this method are given in section 4.3.1.

The correlation between two signals is a standard approach to feature detection as well as a component of more sophisticated techniques. Correlation can be implemented in either the spatial domain or the frequency domain.

The correlation of two functions $f(x, y)$ and $h(x, y)$, both of size $M * N$, is defined as:

$$f(x, y) \circ h(x, y) = (1/MN) \sum_{m=0}^{M-1} \sum_{n=0}^{N-1} f^*(m, n)h(x + m, y + n); \quad (3.6)$$

where f^* is the complex conjugate of f . Initially the correlation was implemented in the spatial domain on the CT scan images, but since the images involved in the correlation were too large for computational efficiency (981 *900 pixels), the correlation was implemented in the frequency domain.

Let $F(u, v)$ and $H(u, v)$ denote the Fourier transforms of $f(x, y)$ and $h(x, y)$, respectively. The correlation theorem states that spatial correlation, $f(x, y) \circ h(x, y)$,

and the frequency domain product, $F^*(u, v)H(u, v)$, constitute a Fourier transform pair [18]. This result, formally stated is:

$$f(x, y) \circ h(x, y) = F^{-1}(F^*(u, v)H(u, v)) \quad (3.7)$$

This states that correlation in the spatial domain can be obtained by taking the inverse Fourier transform of the product $F^*(u, v)H(u, v)$, where F^* is the complex conjugate of F . It is assumed that all functions have been properly extended by zero padding. Zero padding means extending the image to a size that is a power of 2 by adding pixels of value zero.

Rotation Angle Estimate θ_e

In order to find the rotation angle estimate θ_e , the angle between the two upper edges of the skull must be found. Since the upper edge of the skull (Fig. 4.4) is approximately a straight line, its slope with respect to the horizontal is used as the rotation angle of the head. Once the slopes of the upper edges for the two images, I_1 and I_2 , are determined, then the difference angle θ_e between the two upper edges can be determined. This value is the estimate of the rotation angle, θ_e . This is the angle the skull has rotated between the image taken at $tm1$ and $tm2$.

Optimize the Parameters

After estimates for the translation and rotation parameters are obtained (s_e, t_e, θ_e), the values are optimized over a range of values given by $\theta_e \pm 10\%$, $s_e \pm 10\%$ and t_e

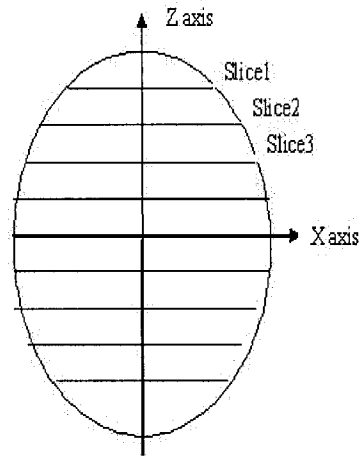


Figure 3.3: *The theory of how to interpolate the slices.*

$\pm 10\%$. The optimization is implemented by minimizing the standard deviation of the image created by taking the difference between the reference image, I_1 and the registered image, I_2 . The final values s , t and θ are the results of this optimization.

3.3.2 Interpolation: for out-of-plane movement(3D)

Consider the image plane to be the X-Y plane and the Z-axis to be perpendicular to the image plane. Any change in position between the two images in the X-Y or image plane is referred to as 2D movement. An example of this type of movement is the head turning to the right. Any change in position out of this plane is considered to be 3D movement. There are two types of 3D movement of concern, the head tilting towards the shoulder and the head nodding. A correction for the movement of the head towards the shoulder was implemented in this thesis while a correction for what is known as a nod was not. Since each slice is taken in the X and Y direction, if 2D movement exists, the pixels still stay in the X and Y plane. When 3D movement

exists, the pixel in any particular slice, eg. slice 2, may move to either adjacent slice, eg. slice 1 or slice 3 (Fig. 3.3). The interpolation method was developed to obtain the new pixels for slice 2 from slice 1 or slice 3.

Once the rotation angle is calculated, the displacement caused by the change in position can be calculated. Using equation 4.4, the number of slices required for the interpolation can be calculated. The details are described in section 4.3.2.

3.4 Partial Volume Effect

One major and common problem that appears when segmentation is implemented is the partial volume effect. When the x-ray passes through the center of an object, the backprojected pixel value represents the density of one substance. When the x-ray passes along the edge of an object, the backprojected pixel value represents the combination of the density values of the different substances and the edge. This is called partial volume effect.

When the partial volume effect exists, pixels at the boundary between structures contain a mixture of material, and consequently have an intensity that is intermediate between the intensity values of the structures. It is hard to determine which structure the boundary pixels belong to since part of the pixel belongs to one material and part belongs to another. If the boundary pixel is segmented with the wrong material then the volume calculated from the segmentation will contain an error. Therefore, minimizing the partial volume effect helps to increase the accuracy of the final volume calculation. The boundary of the ventricle in Fig. 3.4a is blurred because the pixels

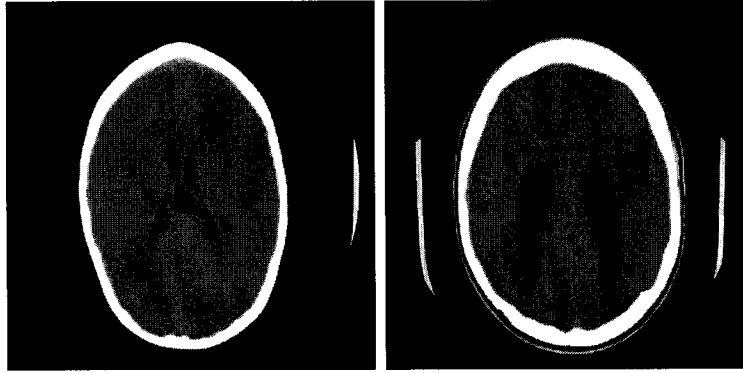


Figure 3.4: *Images with partial volume effect. From left to right (a-b), all images are size 981*900: a. high partial volume effect; b. low partial volume effect.*

in that area represent both the ventricle and the surrounding tissue.

In order to reduce the partial volume effect, it is important to place the boundary pixels in the correct region. To decide to which region the boundary pixels belong, the average gray level of the boundary pixels and the average gray level of surrounding regions are evaluated as follows. First, segment the original image using two different thresholds. Using the first threshold, the segmented region, region 1, does not include the boundary pixels (Fig. 3.5a) and using the second threshold, the segmented region, region2, does include the boundary pixels (Fig. 3.5b). To decide which boundary pixels (Fig. 3.5c) belong to which region, the procedure is as follows:

1. Calculate the average gray value of region 1, $avg1$, and the average gray value of region 2, $avg2$.
2. Calculate the average gray value of these two regions, avg .

$$avg = (avg1 + avg2)/2; \quad (3.8)$$

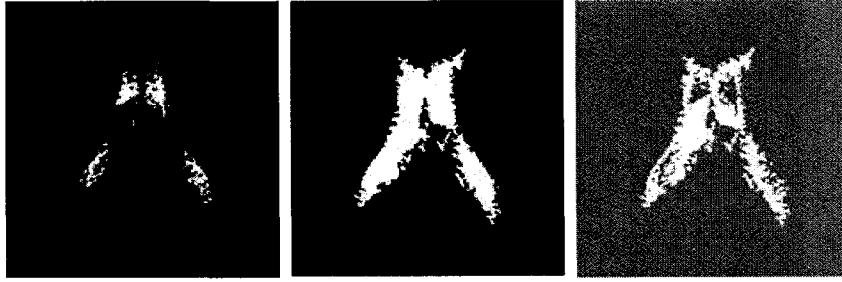


Figure 3.5: *Boundary pixels contain partial volume effect. From left to right (a-c), all images are size 981*900: a. the segmented region of interest which does not contain boundary pixels; b. the segmented region of interest which does contain boundary pixels; c. the boundary pixels.*

3. If $avg1$ is less than $avg2$, check the gray value of each boundary pixel. If the boundary pixel value is less than avg , the boundary pixel belongs to region 1, otherwise it belongs to region 2.

This method is based on the idea that the gray level of the boundary pixel is dependent on the ratio of the volumes of the two substances represented by the pixel. Thus if the threshold is selected as the average of the mean gray levels for each substance, the pixel will be assigned to the region with a mean value closest to its own. This means the pixel is assigned to the region whose substance has the greatest representation in it.

3.5 Volume Calculation

After segmentation, each segmented image is a binary image that only contains ventricles (in white) and background (in black). In order to complete the volume calculation, two variables need to be extracted from the DICOM image's header, pixel

spacing, P_s and slice thickness, S_{thic} . First, the area of each ventricle pixel is obtained from the pixel spacing. The area of each pixel is then multiplied by the number of ventricle pixels, N_p , existing in one slice. Since the slice has a finite thickness, the area of the ventricle, A_{ven} , in the slice is multiplied by the slice thickness to achieve the volume of ventricle in each slice.

$$A_{ven} = N_p * P_s * P_s * S_{thic}. \quad (3.9)$$

P_s is the pixel spacing which corresponds to the width and length of a pixel. S_{thic} is slice thickness which is the height of a pixel.

As the ventricle exists in a number of different slices, all the individual slice volumes must be summed to get the volume of the whole ventricle.

$$V_{tot} = \sum_{i=0}^n A_i. \quad (n = N_{tot\text{slice}}) \quad (3.10)$$

V_{tot} is the total volume of the ventricle. $N_{tot\text{slice}}$ is the total number of slices.

3.6 Measures of Success

For any algorithm implemented or developed, a measure of success of the method is required. The similarity index, S , was used to measure the success of the various segmentation algorithms. To verify the success of the volume calculation algorithm, two methods were used. The algorithm was run on an analytical phantom and the

results compared to the analytical volume. Also a set of physical models was built and placed in the CT scanner and the volume calculated using the algorithm. These results were compared to the known physical volumes.

3.6.1 Similarity Index, S

The evaluation of the three segmentation methods was achieved by calculating the similarity index. The similarity index, S , between two measurements, is defined as the ratio of twice the common area to the sum of the individual areas [24]. Since the slice thickness is constant, only the area of the segmented ventricle is considered when calculating the similarity index.

$$S = 2 * | A1 \cap A2 | / (| A1 | + | A2 |) \quad (3.11)$$

where $A1$ and $A2$ are the number of pixels in the set segmented using methods 1 and 2 respectively. Because the similarity index is the ratio of twice the common area of the segmentation to the sum of the sizes of the individual areas, it is sensitive to both size and location. The similarity index $S \geq 0.7$ indicates excellent agreement [24]. After the index of similarity is calculated for each slice, the average similarity index of each case is calculated using this formula:

$$S_{avg} = \sum_{i=1}^N S_i / N; \quad (N = N_{tot\text{slice}}) \quad (3.12)$$

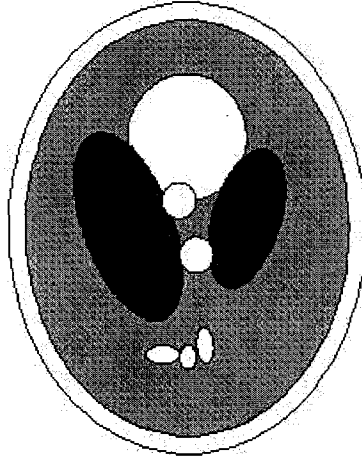


Figure 3.6: *Analytical Phantom.*

where S_{avg} is the average similarity index of each case. S_i is the similarity index of slice i and $N_{totalslice}$ is the total number of slices in one case.

3.6.2 Measures of Success for the Volume Calculation

The success of the volume calculation was measured using both an analytical phantom and created physical models.

Analytical Phantom

The analytical phantom shown in Fig. 3.6 contains ellipsoids with densities intended to represent those of the human head and is a standard used to test algorithms to be used on CT images of the skull [22].

There are ten ellipsoids in the Analytical Phantom. Their parameters are listed in Table 3.1. The volume of each ellipsoid is calculated by finding the area in each slice and then applying equation 3.10. This result was compared with the analytical

Ellipsoid	Coordinates of the Center (x,y,z)	Axis Lengths (A,B,C)	Rotation Angle (deg)	Gray Level
a	(0,0,0)	(0.69,0.92,0.9)	0	2.0
b	(0,0,0)	(0.6624,0.874,0.88)	0	-0.98
c	(-0.22,0,-0.25)	(0.41,0.16,0.21)	108	-0.02
d	(0.22,0,-0.25)	(0.31,0.11,0.22)	72	-0.02
e	(0,0.1,-0.25)	(0.046,0.046,0.046)	0	0.02
f	(0,0.1,-0.25)	(0.046,0.046,0.046)	0	0.02
g	(-0.8,-0.65,-0.25)	(0.046,0.023,0.02)	0	0.01
h	(0.06,-0.065,-0.25)	(0.046,0.023,0.02)	90	0.01
i	(0.06,-0.105,0.625)	(0.56,0.04,0.1)	90	0.02
j	(0,0.1,-0.625)	(0.056,0.056,0.1)	0	-0.02

Table 3.1: Summary of parameters for the 3D Analytical Phantom [22].

volume of an ellipsoid given by equation 3.13.

$$V_{el} = 4/3 * \pi * A/2 * B/2 * C/2 \quad (3.13)$$

The percent error, Err , was obtained using

$$Err = (V_{el} - V_{tot})/V_{el} * 100\%. \quad (3.14)$$

where V_{el} is the volume of the ellipsoid and V_{tot} is the total volume of the ventricle which was defined in equation 3.10.

Physical Phantom Model

A student from Dalhousie created physical models of the ventricles using agar and ice to test the volume calculation algorithm. Two types of physical models were made, simple models and complex models [15][16].

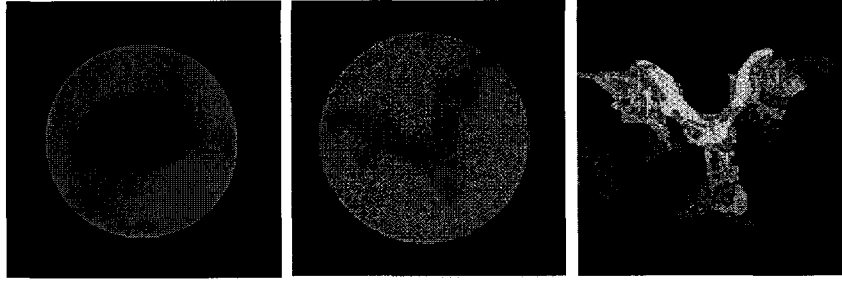


Figure 3.7: *Physical Phantom Models. From left to right (a-c): a. simple model; b. complex model; c. ventricular system model [16].*

The simple models consisted of a cylindrical agar brain which contained a cylindrical fluid-filled space within it (Fig. 3.7a). The reason for choosing agar and water was that their densities closely modeled the densities of the brain and the CSF respectively [4]. The simple models were scanned in the CT scanner at the IWK and the algorithm CSV was executed on the resulting CT image sets. The calculated result was compared with the measured quantity of melted ice. When creating the models, air bubbles existed in the agar. Initially, the air was removed from the simple model. Later models included the air in order to assess the algorithm’s capabilities for dealing with air bubbles, as air is sometimes an issue in clinical scans.

The complex models consisted of a cylindrical agar “brain” which contained a complex fluid-filled space within it which approached the complexity of the structure of the human ventricular system (Fig. 3.7b). A known quantity of water was poured into the ventricular system. For this thesis, the ventricular system from the complex models was segmented out of each slice and the volume was calculated by the volume calculation algorithm, VCAS. Measured results and calculated results were compared and percent error was calculated using equation 3.14.

Chapter 4

Experimental Methods

4.1 Clinical Test Data

The clinical test images were received from the Izaak Walton Killam (IWK) Health Center and were in DICOM format. DICOM stands for The Digital Imaging and Communications in Medicine. It is a standard for the exchange and management of medical images and related information. Medical images are acquired using different modalities such as CT scan devices, magnetic resonance devices or ultrasound devices. A single DICOM file contains a header as well as all of the image pixel data. The header stores information about the patient, as well as all the technical parameters that are set when acquiring the scan. Patient data is removed when the images are anonymized for a research study. Image pixel data can contain information in three dimensions [45]. There are 296 tags included in the header. Examples of technical data are the type of scan, the angle of scan, the field of view (FOV), and the distance

from the source to the detector etc. Field of view, which includes the pixel spacing, pixel thickness, and image size was used in our volume calculation algorithm.

DICOM is the standard image format for receiving scans from a hospital. The image data which was in DICOM format was downloaded from the hard drive of the CT workstation onto a CD disk by the technician at IWK. All patient identification was removed. The anonymized data then was transferred to the Department of Mathematics and Computer Science at Saint Mary's University where the image conversion, algorithm development, and testing were carried out. The DICOM images were converted to JPEG images using software called DICOMWORKS. The JPEG images were then converted to the GIF format and the remaining processing was done using software which we developed for use with the image processing package CVLAB [19]. The software was all written in the C language.

Image data received from the IWK Health Center consisted of 23 clinical cases and data from 16 physical phantom models. Of the 23 clinical cases, fifteen were patients that had had only one CT head scan carried out. The remaining eight cases were patients that had had CT scans of their head taken on at least two different occasions. Each scan consisted of approximately 20 slices. The scans were anonymized but the hydrocephalus diagnosis was documented. Of 16 physical phantom models, 11 cases were scanned at two different angles, 0 and 20 degrees, and 5 cases scanned at four different angles, 0, 5, 10, and 15 degrees. Of the 11 cases, 6 cases were simple models without air, 2 cases were simple models with air, and 3 cases were complex models. Currently, the common slice thickness used for clinical cases of this nature is either 3

mm or 7 mm. As such, slice thickness of 3 mm and 7 mm were used for the physical phantom cases.

4.2 Segmentation

A complete CT scan of the human head taken for the purpose of diagnosing hydrocephalus consists of approximately twenty cross-sectional slices. To calculate the volume of ventricles, the ventricles from each slice are segmented and the area of ventricle calculated in each slice. Since each slice has a thickness, the volume of the ventricle in each slice can be calculated. Then all the volumes are added together. An accurate segmentation method contributes to an accurate volume calculation. To determine the best segmentation method, a number of methods were investigated, such as thresholding [33] [37], region growing [18], the Canny edge detector [9], and clustering [29]. These algorithms were tested on a subset of the clinical images. From the results of these tests it was concluded that thresholding and Region growing were the best suited algorithms for our purpose. These two segmenting methods were used to segment the ventricles from the brain for the rest of the images. This thesis documents the results when these two techniques were applied to our test set of images. To verify the two segmentation methods, the outcome of each of these techniques was compared to that of a manual segmentation and the success was measured by calculating the similarity index (S).

A total of 15 cases were tested. Ten cases were known to have normal ventricles and five were known cases of hydrocephalus. The number of slices in each case ranged

from 20 to 23. The image size was 981 *900 pixels. The distance between slices was 3 mm or 7 mm as documented. All this information was extracted from the associated DICOM tags.

4.2.1 Segmentation by Thresholding

Our thresholding method uses the following algorithm:

1. Get a random sized rectangular patch from the region of interest (completely inside the ventricle), and calculate the mean, m , and the standard deviation, std . The patch was obtained manually using the mouse to delineate the patch and a *GetRegionOfInterest* function in CVLAB [19] to capture it.
2. Set $P_t(x, y) = 255$; if $(m - std) \leq P_o(x, y) \leq (m + std)$; else $P_t(x, y) = 0$.
3. In the previous step, some non-ventricle regions will also be segmented out if they have a grey-level similar to that of the ventricle. To isolate the ventricle, we use a priori knowledge of the position of the ventricle to limit the extent of the region searched for the ventricle.

4.2.2 Segmentation by Region Growing

Our Region growing algorithm works as follows:

1. Get a patch of the region of interest in the same manner as given in Section 4.2.1 and calculate the mean value, m , and standard deviation, std , of this patch.

2. To find the seed or starting pixel, the algorithm checks each pixel in the image of size $M \times N$. The search is started at position $(0, 0)$ and continues until a pixel with a gray value equal to m is found or the search reaches the pixel in position (M, N) . The position of this seed is saved in a vector, V . V is used to store the positions of all the pixels found to be included in the region.
3. For each value in V , the algorithm checks the four neighboring pixels. If the difference between the gray level of these neighboring pixels and m is less than std , the position of the neighboring pixel is put into V .
4. Each time a new pixel position is added to V , the mean and standard deviation of the pixel values referenced by V are recalculated.
5. Steps 3 and 4 are repeated until the size of V does not change.

4.2.3 Segmentation by Manual Method

All of the test images were segmented using a manual method in order to give a basis of comparison for the thresholding and region growing methods. The manual segmentation was supervised by a radiologist.

The steps of the algorithm are described as follows:

1. The radiologist drew the edge of the ventricle on each image slice using Paint software and using the color black (gray value =0).
2. The drawn edge was segmented using a threshold of 0. Each pixel of the modified image was checked. If the gray value of the pixel equalled 0, its gray value was

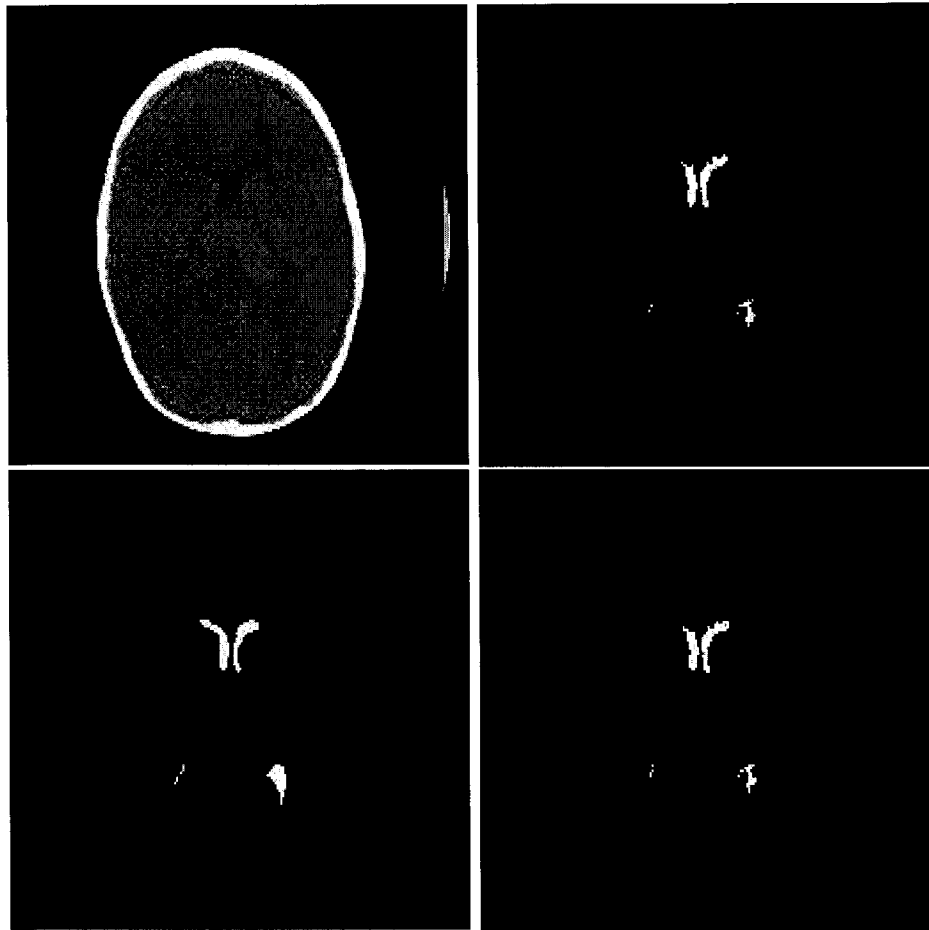


Figure 4.1: *Result images of thresholding, region growing and manual method. From left to right, top to bottom (a-d), all images are size 981*900 pixels: a. original image; b. segmented ventricle using region growing algorithm; c. segmented ventricle using manual method; d. segmented ventricle using thresholding method.*

changed to 255, otherwise it was changed to 0.

3. The segmented edge was closed and a region filling algorithm was applied to form a solid region.

Fig. 4.1 shows an example of the results of thresholding, region growing, and manual techniques after they have been applied to a single slice.

Picture	Dimension	Width	High threshold	Low threshold
Fig. 5.3 a	3	3	50	100
Fig. 5.3 b	15	3	60	280

Table 4.1: Parameters for the Canny Edge Detector.

4.2.4 Canny Edge Detection Algorithm

Another method of automated segmentation that was tested on the ventricles was the Canny edge detection algorithm. The results of this method, an example of which is shown in Fig. 5.3, were not as good as the results from the thresholding and region growing methods.

In the Canny edge detection algorithm, the original image was first smoothed with a Gaussian filter of dimension and width as defined in Table 4.1. Then using the Sobel operator the gradient magnitude and direction were computed at each pixel of the smoothed image. Gradient direction is used to thin edges by suppressing any pixel response that is not higher than the two neighboring pixels along the direction of the gradient. Once the gradient magnitudes are thinned, high magnitude contours are tracked. In the final phase, continuous contour segments are sequentially followed. Contour following is initiated only on edge pixels where the gradient magnitude meets a high threshold, T_h ; once started, a contour may be followed through pixels whose gradient magnitude meets a lower threshold, T_l .

The high and low thresholds, T_h and T_l respectively, were determined as follows: First, the image was smoothed with a Gaussian filter, the Sobel gradient operator was convolved with the smoothed image (Fig. 4.2a). Next, a patch (Fig. 4.2b) of

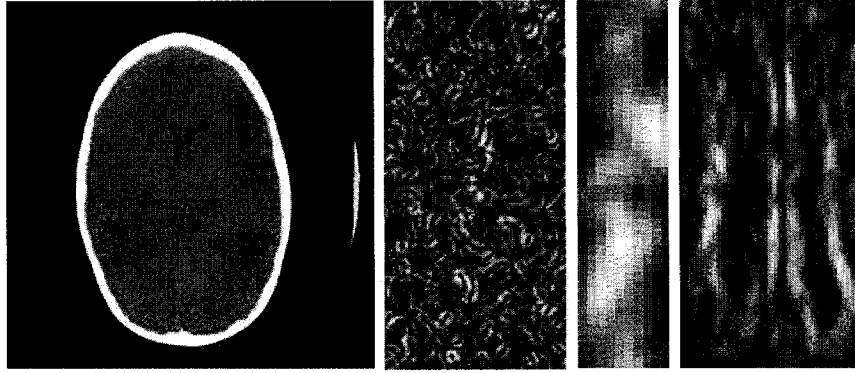


Figure 4.2: *Process images of Canny edge detector. From left to right (a-d): a. original image, image size 981*900 pixels; b. a patch of non-ventricle brain tissue, image size 40*60 pixels; c. a patch of ventricle edge, image size 10*15 pixels; d. a patch inside ventricle, image size 50*75 pixels.*

the non-ventricle part of the head was selected. The average gray value of this patch was used as the high threshold T_h . Similarly, the average gray level values of a patch (Fig. 4.2c) on the edge of the ventricle (Fig. 4.2d) was used as the lower threshold T_l .

4.3 Registration

4.3.1 Affine Transform: for in-plane position change

As mentioned in section 3.3.1, three parameters, translation distances (s and t) and rotation angle (θ) need to be obtained for the affine transform.

Translation Parameter

To get an estimate of the translation parameter, correlation between the image I_1 and I_2 was used to find the shifted distance. An example is shown in Fig. 4.3a of

the image I_1 and in Fig. 4.3b of the image I_2 . Fig. 4.3c is the segmented ventricle from Fig. 4.3b after it has been zero padded. The size of Fig. 4.3c and I_1 are 981*900 pixels before zero padding. Then images in Fig. 4.3a (also zero padded before the transformation) and Fig. 4.3c were each transformed by Fourier transform and the mean value was subtracted. Finally the transformed images were correlated using equation 3.7. The Fig. 4.3d is the result of the correlation shown in the spatial domain. Since no distinct peak could be found this method was abandoned. Instead the Fourier transformed image of I_2 was correlated with the Fourier transformed image of I_1 and a distinct peak was determined as shown in Fig. 4.3e. When an image is correlated with a translated version of itself, the peak appears offset from the center by the amount of the translation. Thus the translation parameters s and t can be determined by this offset in the X and Y directions respectively.

Rotation Angle

The rotation angle was obtained by the following steps:

1. Using the Sobel operator, segment out the edge of the images I_1 and I_2 respectively.
2. Using the manual *GetRegionOfInterest* function in CVLAB [19], isolate the upper edges of the skull from the remaining edges in the segmented images.
3. Find the left most and right most points of each upper edge, and calculate the slope of each upper edge by using these two points. A function for CVLAB was written to implement this.

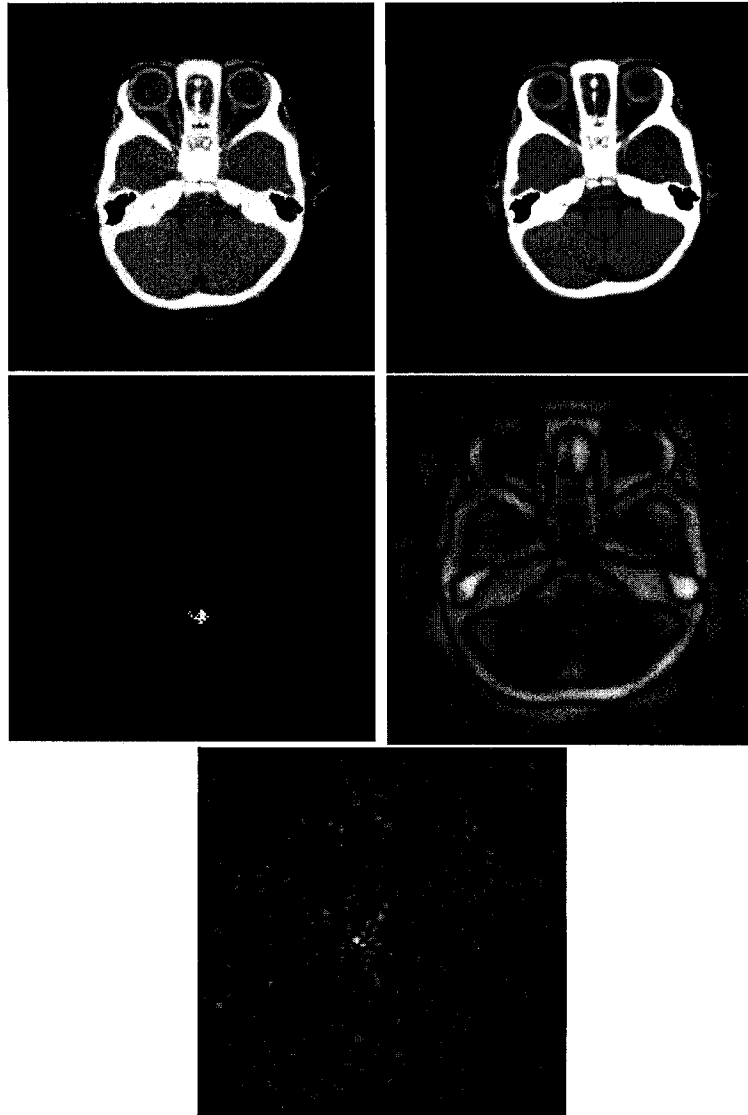


Figure 4.3: *Result images after correlation. From left to right and top to bottom (a-e), the size of images a,b,d,e are 981*900 pixels, and 1024*1024 pixels for image c: a. image at tm1; b. image at tm2; c. the ventricle segmented from b; d. the result image of correlation of b and c; e. the result image of correlation of a and b.*

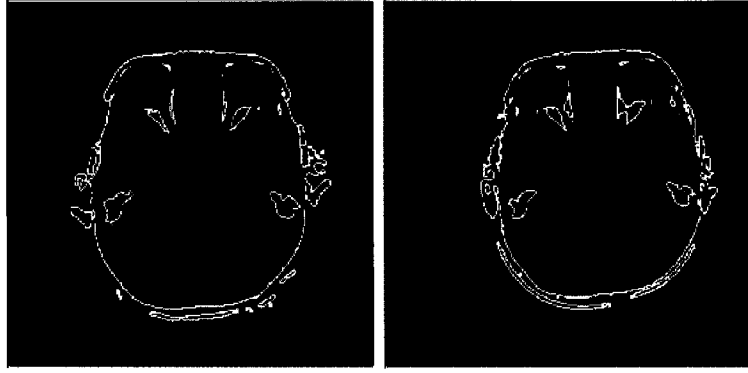


Figure 4.4: Result image after rotation. Left to right (a-b), all image size are 981*900 pixels: a. the edge of Fig. 4.3a; b. the edge of Fig. 4.3b.

4. Using the slopes from step 3, obtain the angle between two upper edges. This is the rotation angle. Function *AngleBTlines* was written to implement this.

Optimize the Affine Transform

The parameters for the affine transform were optimized as follows. For each value between $\theta_e \pm 10\%$, $s_e \pm 10\%$ and $t_e \pm 10\%$, the standard deviation (*std*) of the difference of the original image and the registered image was calculated. The values of θ , s and t which resulted in the minimum standard deviation of the difference image, were selected as the final parameters for the affine transform.

4.3.2 Interpolation: for out-of-plane position change

Even if all the physical machine settings are the same for two CT scans of the same patient taken at two different times, it is possible for the resulting images to still be quite different. One reason for this is a slight change in the position of the patient's head in each scan. This causes the existence of a tilted angle in the CT images and

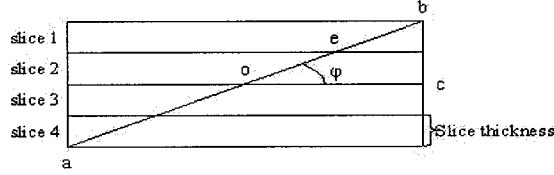


Figure 4.5: *The interpolation of out-of-plane movement: ab is the slice taken at time tm_2 ; slice 1, slice 2, slice 3 and slice 4 are taken at time tm_1 .*

also affects the ventricle volume calculation. In order to reduce the effect of this problem, the images I_2 were registered to the images I_1 .

The eyeball was selected as the landmark for the two sets of images I_1 and I_2 . For images I_1 and I_2 , the first slice in which two eyeballs appear was found. The size of the two eye balls (R_1 and R_2 respectively) in one slice and as well as the distance between the nose and eyeball center, oc , were measured. A program was developed to calculate the distance between any two points. The user was required to choose two points, one was the center point of the eyeball and the other was an edge point of the eyeball. Then the program automatically calculated the size of the eyeball. From these three values, R_1 , R_2 and oc , the angle of head tilt was calculated.

Steps :

1. Calculate the radius of small eyeball, (R_1), radius of large eyeball (R_2) and the distance between the nose and the large eyeball center(oc) (Fig. 4.5).
2. Calculate the angle (agl) of the head tilt at each time period by this formula:

$$\cos\alpha = R_1/R_2; \quad (4.1)$$

$$\sin\beta = R_2 * \text{sqrt}(1 - \cos\alpha * \cos\alpha)/oc; \quad (4.2)$$

$$agl = \arctan(\sin\beta/\sqrt{1 - \sin\beta * \sin\beta}); \quad (4.3)$$

3. Do the above steps for images I_1 and I_2 respectively and obtain the tilt angle (φ) between these two images.
4. Calculate the length of line bc using the line oc and φ (Fig. 4.5). Then obtain the number of slices needed to interpolate by the following equation:

$$N_{inter} = bc/S_{thic}; \quad (4.4)$$

where N_{inter} is the number of slices need for the interpolation and S_{thic} is the slice thickness.

5. The slice ab can be obtained by interpolating between previous and later slices: slice ob can be obtained from slice 1 and slice 2, slice oa can be achieved from slice 3 and slice 4 (Fig. 4.5). For example, the pixels in position along the slice oe of the generated new slice were obtained from slice 2 and the pixels in position along the slice eb were obtained from slice 3 and so on.

4.4 Partial Volume Effect

The method developed to reduce the partial volume effect uses a combination of the thresholding method and the region growing method. It automatically segments out all the ventricle pixels which include the partial volume effect and then includes them

in the appropriate region depending on the average pixel value of the boundary pixels and the surrounding region pixels.

The main method includes the following steps:

1. Segment out the ventricle (Fig. 4.6a) by the thresholding method using threshold, T_1 , and save the positions of these pixels in vector V_1 . The threshold T_1 is the average pixel value of a region totally inside the ventricle. This region is obtained manually using the *GetRegionOfInterest* function.
2. Segment out the ventricle (Fig. 4.6b) using the thresholding method again, this time using threshold, T_2 . Save the position of these pixels in vector V_2 . The threshold T_2 is the average pixel value of a region which includes the whole ventricle. This region is also obtained manually using the *GetRegionOfInterest* function and includes the whole ventricle and part of the surrounding tissue.
3. Check the four neighboring pixels of each pixel in V_1 . Push the neighboring pixel into V_1 if it is also in V_2 .
4. Do step 3 again for the new element in V_1 until the size of V_1 does not change. Fig. 4.6c shows an example of the resulting image after this region growing has been completed.
5. To obtain the boundary pixels which cause the partial volume effect, the image obtained from step 1 (Fig. 4.6a) is subtracted from the image obtained in step 4 (Fig. 4.6c). In order to decide which region these boundary pixels belong to, check the boundary pixel value. If the pixel value is less than $90=(60+120)/2$,

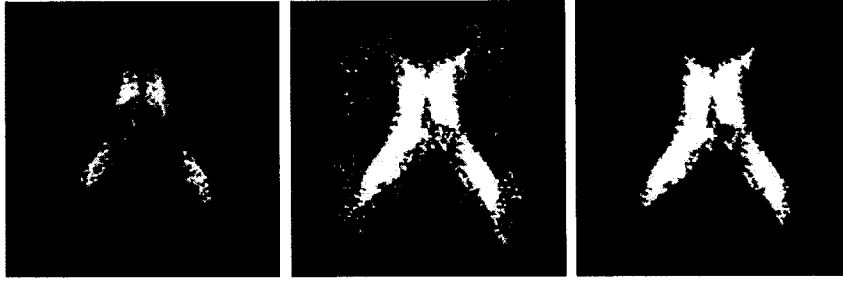


Figure 4.6: *Patial Volume Effect Correction. Left to right (a-c), all image size are 981*900 pixels: a. and b. are images segmented by thresholding method by two different thresholds; c. the image after region growing.*

the pixel belongs to the ventricle, otherwise it does not. 120 is the average pixel value for tissue inside the skull and surrounding the ventricle and 60 is the average pixel value for the ventricle as given in section 3.1.1.

A second method of reducing the partial volume effect was briefly tested and subsequently not used as it was found to be ineffective. This method used a Gaussian filter to smooth the image before thresholding. Then the original image and the smoothed image were subtracted to obtain the pixels affected by the partial volume effect.

4.5 Volume Calculation

4.5.1 Volume Calculation Across Slices (VCAS)

Once the segmented images without parital volume effect have been obtained, the next step is to calculate the volume of the ventricles. The process of the ventricle volume estimation goes as follows:

1. Count the number of white pixels of each slice, N_p . After segmentation, the image is binary.
2. Calculate the area of white pixels for each slice according to equation 3.9.
3. Add up all the slices using equation 3.10.

To verify the accuracy of the volume calculation method, the method was tested on both an analytical phantom and physical models.

4.5.2 Analytical Phantom

In the analytical phantom, each ellipsoid has three different axis: A , B and C . In order to obtain the length of the axis in mm, the per unit values given in Table 3.1 were scaled using the following formula:

$$L_{new} = L_{org} * P_s * N; \quad (4.5)$$

L_{new} is the new length of the axis in mm after scaling. L_{org} is the original length. P_s is the pixel spacing and N is the image size. Since the pixel spacing of the clinical images was 0.410156 mm, an assumption was made that the pixel spacing of the ellipsoid was equal to 0.410156 mm and the size of the image was 512 *512 pixels. The actual volume of each ellipsoid was calculated according to the standard volume formula (equation 3.13).

To test our volume calculation algorithm, the whole ellipsoid was divided into a number of slices perpendicular to the B axis. Three slice thicknesses were tested: 3

mm, 7 mm and 10mm. For each slice thickness, the ellipsoid volume was estimated using the VCAS algorithm and the results were compared with the actual volume of the ellipsoid calculated using equation 3.13. The percent error was also calculated.

4.5.3 Physical Phantom

Physical phantom models [15] [16] were created and the volume calculation algorithm was tested on these models and a percentage error was calculated. An undergraduate student from Dalhousie, created 8 simple models at 2 angles, 3 complex models at 2 angles and 5 complex models at 4 angles for us to test the volume calculation algorithm. The 8 simple models consisted of 6 simple models without air and 2 simple models with air, since in real images it is possible that small air pockets will exist. The reason for creating the complex model was that the structure of the complex model was much closer to the shape of the ventricle and thus more thoroughly challenged the algorithm.

Each set of simple models was scanned four independent times, twice using slice thickness and spacing of 3 mm x 3 mm for 2 different scan angles (0 and 20 degrees), and twice using 7 mm x 7 mm for 2 different scan angles (0 and 20 degrees). In order to assess the algorithm's reliability and the potential for eliminating the problem of comparisons between varying head scanning angles, 4 different angles (0, 5, 10, 15 degrees) were each used for another 5 complex models.

From a clinical point of view, there is inevitably some air in the ventricles. Ideally, this air should not be excluded from the measured ventricular volume. That was the

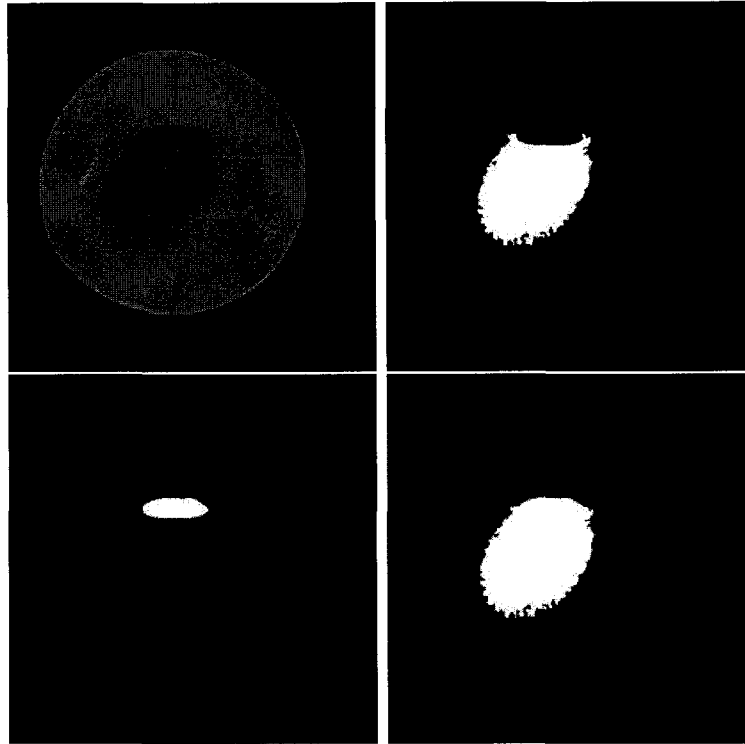


Figure 4.7: *Segmented images for Physical Phantom. From left to right, top to bottom (a-d), all image size are 981*900 pixels: a. the original image; b. segmented water; c. segmented air; d. result image obtained by adding b and c together.*

reason the simple air models were created and the air was segmented out. In the simple air models, since the grey level for the air is equal to zero, to segment out air it was just necessary to set the threshold equal to zero.

$$\text{if } P_o(x, y) = 0, \quad \text{Set } P_t(x, y) = 255; \quad \text{else } P_t(x, y) = 0.$$

The air is assumed to exist in the ventricle so the final ventricle volume was calculated using the total of the two segmented areas. An example is shown in Fig. 4.7. After the volume of the physical phantom was calculated by the VCAS algorithm,

it was compared to the known actual volume and the percentage error was calculated.

4.6 Combination of All Algorithms: CSV

In previous chapters, segmentation, partial volume effect and volume calculation were discussed. We know the segmentation method was used to extract the ventricle from the CT image and the volume calculation method was applied to the segmented images to achieve the volume of the ventricle. The partial volume effect method was used to reduce the segmentation error to obtain a more accurate segmentation of the image. All these methods were introduced separately. Now it is a good time to link them all together into a single method referred to as CSV, for “Combination of Segmentation and Volume”. It works as follows:

1. If the image I_2 was translated or rotated with respect to image I_1 , register I_2 to I_1 .
2. Segment the registered image using the thresholding method. The threshold was the average value of a patch taken from inside the ventricle. All pixel positions were saved in a vector V_1 .
3. Segment the registered image using the thresholding method again. This time the threshold is the average value of the region including the ventricle. Save all pixel positions in a vector V_2 . In this situation, the boundary pixels of the ventricle and noise pixels are all included in the segmented region.
4. Use the Region growing algorithm, for each pixel in V_1 check its four neighboring

pixels, if the four neighboring pixels also appear in V_2 , put these pixels into V_3 . The vector V_3 contains all the boundary pixels of the ventricle without any noise pixels.

5. Check each boundary pixel whose position was saved in V_3 . In the image I_1 , if the gray value of the boundary pixel was less than the average value (avg) of the average value of ventricle ($avg1$) and the average value of grey brain tissue ($avg2$) (equation 3.8), put these boundary pixel positions into V_1 . Finally, the pixels in V_1 belong only to the segmented ventricle and the partial volume effect has been minimized.
6. Count the number of pixels in each segmented slice image and calculate the volume of the ventricle in each slice by multiplying the number of pixels by the pixel area and slice thickness (equation 3.9).
7. Finally, obtain the total volume by adding all sub-volumes up (equation 3.10).

Chapter 5

Experimental Results

5.1 Results for Segmentation

To measure how well the results of the two methods, thresholding and region growing, correspond to the manual method, the similarity index was calculated as mentioned in section 3.6.1. A total of 15 cases were tested and all the results are listed in Table 5.1. Ten of these cases were known to have normal ventricles and five cases were known to have been diagnosed with hydrocephalus. Each case consisted of twenty to twenty-three slices. Some of these slices included part of the ventricle and some did not. The slice thickness in the clinical data was different for each case, some cases were 3.00 mm, some were 7.00 mm. The clinical images were changed to binary images (background in black and ventricle in white) after the segmentation.

Then the similarity index was calculated for three pairs of methods: thresholding and manual methods, region growing and manual methods, and thresholding and

Case number	Similarity Index of Thresholding vs Manual	Similarity Index of RegionGrowing vs Manual	Similarity Index of Thresholding vs RegionGrowing
1	0.83	0.82	0.92
2(hy)	0.78	0.78	0.90
3	0.75	0.74	0.85
4	0.84	0.73	0.80
5	0.83	0.81	0.88
6(hy)	0.76	0.78	0.78
7	0.77	0.78	0.97
8(hy)	0.81	0.83	0.98
9(hy)	0.78	0.80	0.94
10	0.80	0.81	0.96
11	0.77	0.77	0.82
12	0.74	0.75	0.79
13(hy)	0.82	0.80	0.91
14	0.79	0.79	0.83
15	0.78	0.76	0.79
Overall Avg	0.79	0.78	0.87

Table 5.1: *Similarity Index for 15 Clinical Cases.*

region growing. The similarity index of these 15 cases were all above 0.7, which indicates an appropriate segmentation was achieved. The results also show that the segmentation algorithm works equally well on both hydrocephalus cases and non-hydrocephalus cases.

5.1.1 Thresholding

First, the images were segmented out by using thresholding and manual method. Then the results from the thresholding method were compared to the results of the manual method by calculating the similarity index. In the Fig. 5.1a, each point represents the average similarity index for each cases. The range of the average

similarity index for each case was from 0.74 to 0.84 as listed in second column of the Table 5.1.

5.1.2 Region growing

Similarly the similarity index resulting from the comparison of the region growing and the manual methods was calculated for each slice in each case. In Fig. 5.1b, each point represents the average similarity index for each case. The average similarity index for each case varied from 0.73 to 0.83 as listed in third column of the Table 5.1.

5.1.3 Thresholding and Region Growing

After the comparisons between the thresholding and manual methods, and region growing and manual methods were completed, the results of the thresholding and region growing methods also were compared by calculating the similarity index. Fig. 5.1c shows the range of the similarity index was from 0.78 to 0.98 as listed in fourth column of the Table 5.1.

Excellent results were obtained with both the region growing and the thresholding methods. All the calculated similarity indices were greater than 0.7. Specifically, in Fig. 5.1d, the average similarity index between the threshold and manual method for the fifteen measured cases was 0.79. The average similarity index between the region growing and manual methods was 0.78 and the average similarity index between thresholding and region growing of 15 cases was 0.87. These values indicate the

thresholding and region growing methods give highly consistent results.

In some cases, the reason for the lower similarity index is the partial volume effect. Since a similarity index equal to or greater than 0.7 indicates a good match [24], our similarity index values which fall in the range of 0.73 to 0.98 indicate that the thresholding and region growing methods are reliable for segmenting the ventricle from CT scan image.

5.1.4 Sensitivity of the Thresholding

The sensitivity of the threshold was calculated for each slice and the average sensitivity for each case is equal to $\pm 10.67\%$ (Fig. 5.2). This means that if the threshold used for the segmentation is varied by $\pm 10.67\%$, the total number of pixels segmented won't change. Although the difference between the average gray value of the ventricle and the average gray value of the surrounding tissue is large, the partial volume effect makes it difficult to pick the threshold. So a sensitivity equal to $\pm 10.67\%$ is acceptable. The higher the sensitivity, the more robust the thresholding.

5.2 Results for Canny Edge Detector

The output of the Canny edge detector was a very rough edge around the ventricles and many other edges in the image (see Fig. 5.3). The resulting output was very noisy. This made it very difficult to segment the ventricles. The Canny edge detection algorithm was abandoned. The reason the Canny edge detection failed on CT images of the head was that this algorithm not only involves the gray value of the edge

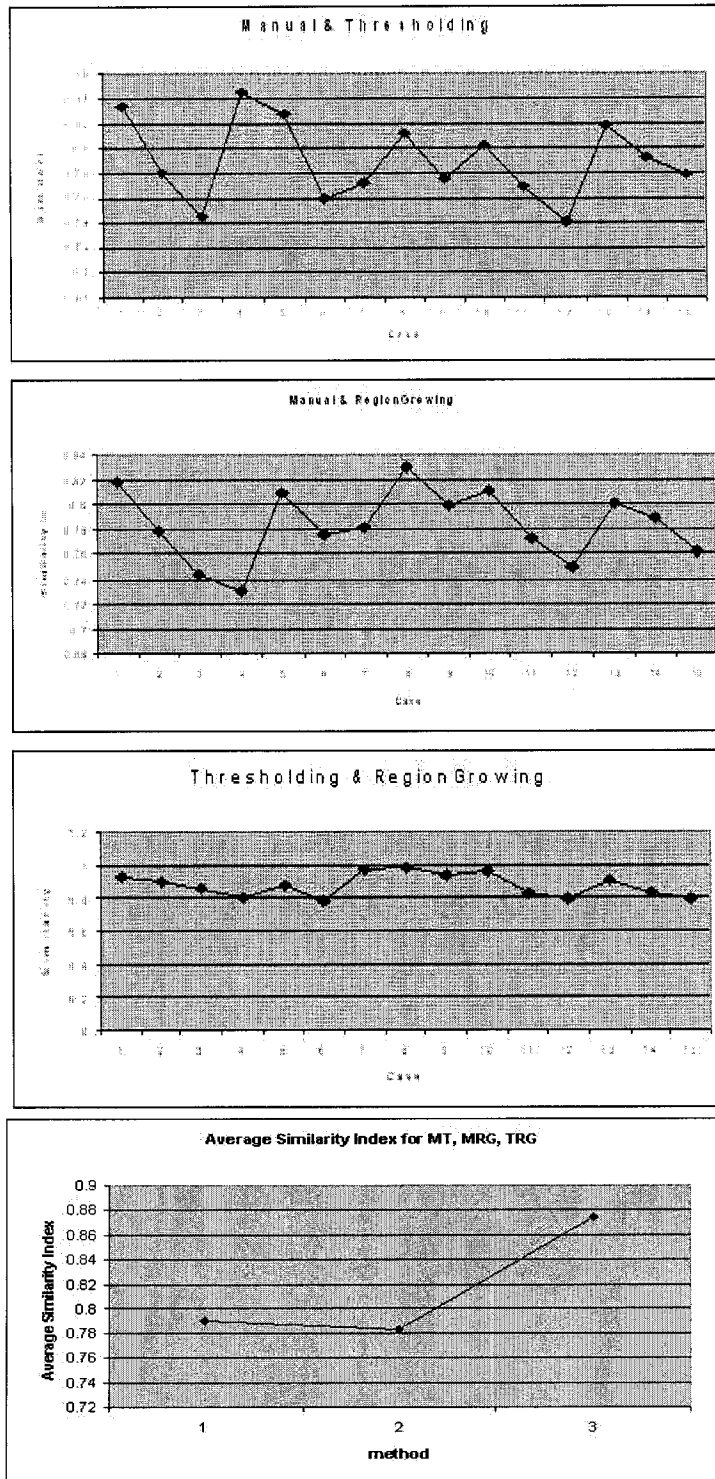


Figure 5.1: Graphs of the similarity index for 15 clinical cases. From top to bottom (a-d): a. manual vs threshold; b. manual vs region growing ; c. Threshold vs Region growing; d. average similarity index of three methods.

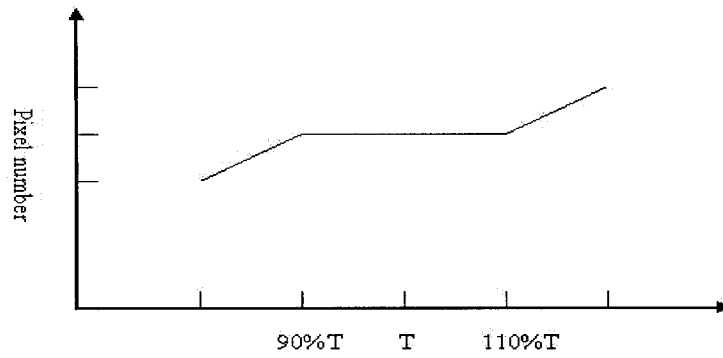


Figure 5.2: *Threshold sensitivity.*

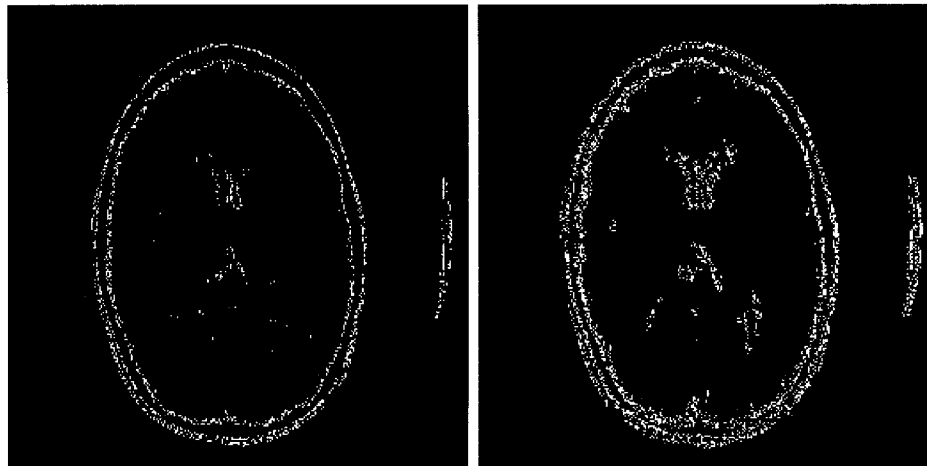


Figure 5.3: *Results for Canny Edge Detector. From left to right (a,b), all images are size 981*900 pixels: a. image segmented by canny edge detector with Gaussian filter dimension=3, width=3, high threshold=50, low threshold=100; b. image segmented by canny edge detector with Gaussian filter dimension=15, width=3, high threshold=60, low threshold=280.*

but also involves the texture of the edge. The edge between the ventricles and the surrounding tissues is not distinct enough to get a good segmentation based on edge information alone. Fig. 4.2d shows the texture of the edge clearly. In order to extract more edge segments, the dimension of the Gaussian filter was increased, but when the dimension increased, the noise also increased. Segmentation based on the texture was not explored in this thesis, but it is a potential topic for future research.

5.3 Results for Registration

The registration algorithms were tested on the eight clinical cases that included two scans taken at different times but of the same patient. We call these double cases. Five of these cases were known to have normal ventricles and three cases were known to have hydrocephalus. The volumes of these eight registered and segmented cases were calculated and listed in Table 5.7. The results of the registration techniques are illustrated by the examples given in Fig. 5.4 and Fig. 5.5.

5.3.1 Results for Affine transform (2D)

Fig. 5.4a and Fig. 5.4b are the images for the same patient taken at two different times. Fig. 5.4c is the results image after the optimized affine transform has been applied. The skull in Fig. 5.4b was shifted -32 pixel positions along the x axis, -9 pixel positions along the y axis and rotated 3 degree with respect to Fig. 5.4a. So the range of translation distance in the x direction used for optimization was -35 to -29 pixel positions and in the y direction was -10 to -8 pixel positions. The range for

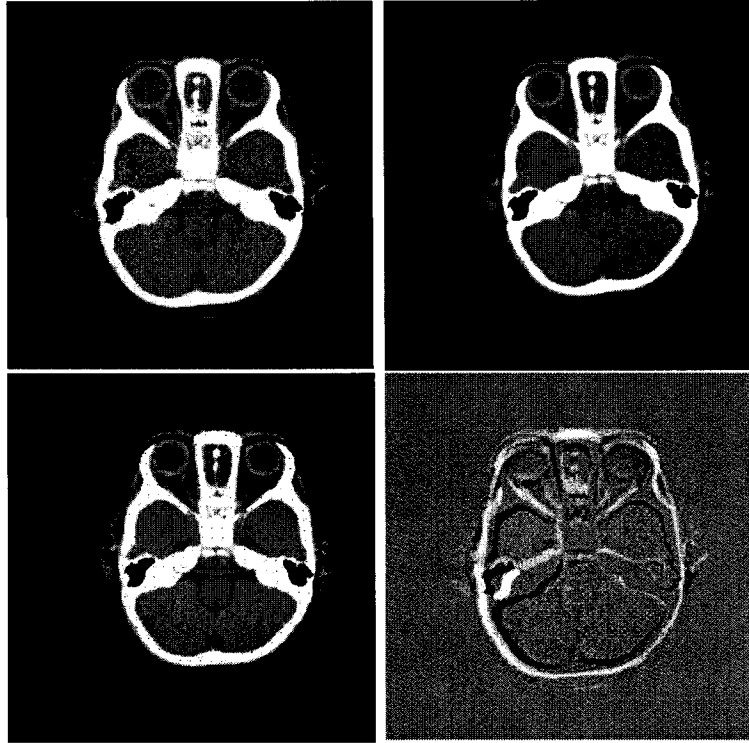


Figure 5.4: *Results of Affine Transform. From left to right and top to bottom (a-d), all image sizes are 981*900 pixels: a. the image at tm1; b. the image at tm2; c. the registered image of b; d. the difference image of a. and c.*

the rotation angle was 2 to 4 degrees. The optimized value for s and t were -31 pixel positions and -9 pixel positions respectively. Image I_2 was registered according to each value of s_e , each value of t_e and each value of θ_e . The difference between I_1 and the registered image was obtained and the standard deviation of this difference image was calculated each time. When the standard deviation was minimal, the values of s_e , t_e and θ_e were taken as optimal. Fig. 5.4d is the difference of Fig. 5.4a and Fig. 5.4c. The standard deviation of Fig. 5.4 d is 24.56 which is minimal.



Figure 5.5: *Result after interpolation. From left to right (a-c), all image sizes are 981*900 pixels: a. image taken at time tm_1 ; b. image taken at time tm_2 ; c. image after interpolation.*

5.3.2 Results for Interpolation (3D)

The image in Fig. 5.5a was I_1 and the image in Fig. 5.5b was I_2 . The eyeballs in the two images show that the position of the patient's head was shifted between the scans. Using the eyeball sizes in each image, the difference angle between these two images can be calculated (see Section 4.3.2). When the difference angle has been obtained, the head in Fig. 5.5b can be transformed back to the same position as the head in Fig. 5.5a. The head in Fig. 5.5c is the result after the interpolation algorithm has been applied. Judging from the eyeballs in Fig. 5.5a and Fig. 5.5c, the shift in angle has been corrected.

5.4 Results for Volume Calculation

5.4.1 Analytical Phantom

As discussed in Section 4.5.2 and 3.6.2, the volume calculation algorithm (VCAS) was tested on an analytical phantom (Fig. 3.6). The analytical phantom is a model of

Length of three axis	ActualVolume (mm ³)	SliceThickness (mm)	Calculated Volume(mm ³)	Error %
A=0.69 B=0.92 C=0.9	2.77E6	3 7 10	2.79E6 2.77E6 2.76E6	0.69 0.14 0.39
A=0.6624 B=0.874 C=0.88	2.47E6	3 7 10	2.48E6 2.46E6 2.48E6	0.44 0.24 0.35
A=0.41 B=0.16 C=0.21	6.68E4	3 7 10	6.72E4 6.63E4 6.71E4	0.61 0.77 0.50
A=0.31 B=0.11 C=0.22	3.64E4	3 7 10	3.60E4 3.67E4 3.66E4	0.77 0.92 0.81
A=0.046 B=0.046 C=0.046	471.99	3 7 10	479.75 465.88 467.21	1.60 1.30 1.00
A=0.56 B=0.04 C=0.1	10.86E3	3 7 10	10.78E3 10.81E3 10.93E3	0.74 0.30 0.65
A=0.056 B=0.056 C=0.1	1520.66	3 7 10	1557.21 1501.59 1498.77	2.40 1.30 1.40
A=0.046 B=0.023 C=0.02	102.61	3 7 10	99.72 104.61 100.84	2.80 1.95 1.70
A=0.046 B=0.046 C=0.046	471.99	3 7 10	479.75 465.88 467.21	1.60 1.30 1.00
A=0.046 B=0.023 C=0.02	102.61	3 7 10	99.72 104.61 100.84	2.80 1.95 1.70
Avg				1.14

Table 5.2: *Calculated volume of analytical phantom.*

the head commonly used in medical image analysis. The volume calculation algorithm was first tested on the analytical phantom.

Table 5.2 contains the volume calculation results for the ten ellipsoids in the phantom. The table consists of length of three axis, actual analytical volume of the ellipsoid, slice thickness, calculated volume by VCAS algorithm and percent error between the analytical volume and the volume obtained from the VCAS algorithm. The percent error is in the range of 0.14% to 2.8%, which is consistently less than 3%. A 5% error is considered acceptable in the literature [4][5][8].

5.4.2 Physical Phantoms

As discussed in section 4.5.3, the volume calculation algorithm (VCAS) was tested on a set of physical models with measured volumes.

The final results of these tested models were organized in four tables. Table 5.3 shows the results of the six simple models. The results of the 2 simple air models were summarized in Table 5.4 and Table 5.5 contains the results of the three complex models. The tables (Table 5.3, Table 5.5) for the models without air have four columns. The first column is the actual measured volume for the model, the second column gives the slice parameters which are slice thickness and slice spacing, the third column is the volume calculated by the volume calculation algorithm (VCAS) and the last column is the percent error of the calculated volume based on the actual volume.

The overall average percent error for the set of simple models was 2.52% and the overall average percent error for the 3 mm x 3 mm images was 2.71% and was 2.33%

Simple model actual volume (ml)	Slice parameters[slice thickness (mm) x slice spacing (mm)]	Calculated volume (ml)	Error %
11.5	3x3	11.2	2.61
	7x7	12.0	4.35
	3x3 at 20 degree	10.9	5.22
	7x7 at 20 degree	11.8	2.61
	average	11.5	3.70
16.5	3x3	15.9	3.60
	7x7	16.1	2.40
	3x3 at 20 degree	16.4	0.60
	7x7 at 20 degree	16.7	1.09
	average	16.3	1.92
25.5	3x3	25.9	1.57
	7x7	25.8	1.18
	3x3 at 20 degree	25.0	1.96
	7x7 at 20 degree	26.0	1.96
	average	25.7	1.67
32.5	3x3	31.5	3.00
	7x7	32.0	1.50
	3x3 at 20 degree	33.4	2.70
	7x7 at 20 degree	33.3	2.46
	average	32.5	2.42
58.0	3x3	56.3	2.86
	7x7	56.3	2.93
	3x3 at 20 degree	60.0	3.45
	7x7 at 20 degree	59.0	1.72
	average	57.9	2.70
60.0	3x3	59.2	1.33
	7x7	58.5	2.50
	3x3 at 20 degree	62.2	3.67
	7x7 at 20 degree	62.0	3.33
	average	60.5	2.69
Overall Avg Error			2.52

Table 5.3: *The calculated ventricular volumes of the simple models compared to the actual simple model volumes based on images for various slice parameters [16].*

Simple model: volume of water(ml)	Slice parameters [slice thickness (mm)x slice spacing(mm)]	Calculated volume of water (ml)	Error %	Estimated volume of air (ml)	Calculated volume of air (ml)	Error %
55.0	3x3	53.7	2.36	5	4.80	4.00
	7x7	54.5	0.91		5.10	2.00
	3x3 at 20 degree	55.3	0.55		4.89	2.20
	7x7 at 20 degree	54.3	1.27		5.20	4.00
	average	54.5	1.27			3.05
76.0	3x3	75.1	1.18	2	1.91	4.50
	7x7	73.6	3.16		2.01	0.50
	3x3 at 20 degree	77.9	2.50		1.94	3.00
	7x7 at 20 degree	74.0	2.63		2.10	5.00
	average	75.2	2.37		2.00	3.25
Overall Avg Error			1.82			3.15

Table 5.4: The calculated volumes of both water and air for the simple models based on various slice parameters compared to the actual water volumes and estimated actual air volumes [16].

Complex model actual volume (ml)	Slice parameters[slice thickness (mm) x slice spacing (mm)]	Calculated volume (ml)	Error %
61	3x3	61.1	0.23
	7x7	62.7	2.79
	3x3 at 20 degree	59.0	3.28
	7x7 at 20 degree	58.6	3.93
	average	60.4	2.56
63	3x3	61.4	2.54
	7x7	64.8	2.86
	3x3 at 20 degree	62.3	1.10
	7x7 at 20 degree	65.0	3.17
	average	63.4	2.42
69.8	3x3	71.6	2.58
	7x7	72.0	3.15
	3x3 at 20 degree	72.7	4.15
	7x7 at 20 degree	69.5	0.43
	average	71.5	2.58
Overall Avg Error			2.52

Table 5.5: The calculated ventricular volumes of the complex models based on images with various slice parameters compared to the actual ventricular volumes [16].

for the 7 mm x 7 mm images. These percent errors show that the slice thickness does not significantly affect the volume calculation.

The overall average percent error for calculations of water volume for the simple air models was 1.82%, and the overall average percent error for calculations of air volume for the simple air models was 3.15%.

The overall average percent error for the complex models was 2.52%. The accuracy of the ventricular volumes calculated by the volume calculation algorithm was controlled within 5.2%. Although 5.2% is above 5%, this error rate was also well within the accepted values for error rates documented in the literature, which range between 4% and 16% [40].

All of the above physical models were scanned at two different angles: zero and twenty degrees. To check if changing the scan angle effects the results or not, five complex models were scanned at four different angles: 0 degrees, 5 degrees, 10 degrees and 15 degrees. The results are given in Table 5.6.

The overall average error of these five cases was 2.62% which is within 5%. From this it can be concluded that the changes in the scan angle of up to 20 degrees, or the clinically relevant range, does not affect the volume calculation.

5.4.3 Clinical Double Cases

A total of eight clinical double cases were tested and five were known to have normal ventricles and three were known to have hydrocephalus. The results are given in Table 5.7. In this table, there are six columns: case name, ventricle volume at time $tm1$,

Actual Volume (ml ³)	Angle (degree)	Calculated volume (ml ³)	Error %
102	0	104.1	2.07
	5	104.8	2.79
	10	103.4	1.37
	15	105.2	3.12
	average		2.34
112	0	115.6	3.19
	5	113.8	1.65
	10	115.2	2.89
	15	115.6	3.18
	average		2.73
130	0	134.8	3.69
	5	135.0	3.86
	10	135.6	4.33
	15	134.9	3.78
	average		3.92
101	0	103.7	2.70
	5	103.4	2.33
	10	104.6	3.54
	15	102.0	1.00
	average		2.39
88	0	90.2	2.49
	5	89.9	2.24
	10	89.3	1.43
	15	87.4	0.73
	average		1.72
Overall Avg Error			2.62

Table 5.6: *Volume of complex physical models taken at four different angles [15].*

case name	Ventricle volume at $tm1(mm^3)$	ventricle volume at $tm2(mm^3)$	Old Error %	New ventricle volume at $tm2 (mm^3)$	Error %
4j	5.20	5.19	0.16	5.16	0.78
2j(hy)	94.16	178.65	89.73	127.84	35.80
5j	26.95	31.21	15.78	27.98	3.83
BH	6.14	8.18	33.37	6.47	5.41
KC	6.96	7.37	5.83	7.15	2.76
KF(hy)	59.73	92.04	54.09	74.52	24.77
TGT(hy)	7.23	13.53	87.11	9.88	36.56
CM	10.19	12.85	26.08	10.70	4.97

Table 5.7: Results of volume calculation for eight clinical double cases.

ventricle volume at time $tm2$, old error, new ventricle volume at time $tm2$ and error. In order to illustrate the significance of registering the images, two extra columns have been added to Table 5.7. Column 3 gives the result of calculating the volumes without registering the images and column 4 gives the percentage difference between the volumes at $tm1$ and $tm2$ calculated in this manner. Column 5 gives the ventricle volume using the complete algorithm including registration, CSV.

Table 5.7 shows that before the images were registered the difference in ventricle volume calculated at $tm1$ and $tm2$ was tremendously large. After the interpolation across the slices, the difference of the normal ventricle volumes at $tm1$ and $tm2$ is less than 5.5%. This is consistent with the error of the volume calculation methods for the created physical models. In cases where hydrocephalus was diagnosed, the change in volume was greater than 20%. This indicates that the algorithm (CSV) would be a valuable aid in diagnosing hydrocephalus.

Case	volume of ventricle (mm ³)	volume of skull (mm ³)	Ratio (%)
1	20444.3	4417350	0.46
2(hy)	32523.4	6670420	0.49
3	24239.2	6124920	0.40
4	22085.6	6861690	0.32
5	22573.5	7214850	0.31
6(hy)	34588.9	7567210	0.46
7	20203.5	6346060	0.32
8(hy)	29714.3	6413705	0.46
9(hy)	28232.7	5957040	0.47
10	27213.2	6124920	0.44
11	22158.3	6891720	0.32
12	24335.5	7014520	0.35
13(hy)	34588.9	7567210	0.46
14	23220.5	6562060	0.35
15	26729.5	6486150	0.41

Table 5.8: *Ratio of ventricle to skull for 15 clinical cases.*

5.4.4 Ratio of Ventricle to Skull

Besides using the volume calculation algorithm to estimate the ventricle volume change due to the hydrocephalus, the ratio of ventricle volume to skull volume was also calculated. As can be seen from the results listed in Table 5.8 this ratio was not a good indication of disease. Both the ventricle and the skull enlarge in some hydrocephalus cases so that the change in ratio was minimal (Table 5.8). Therefore, it was determined that this measure was not a good aid in the diagnosis of hydrocephalus.

Chapter 6

Conclusion

In this thesis, we have developed a method to estimate the volume of the cerebral ventricles to aid in the diagnosis of hydrocephalus. This method can be divided into two main steps: segmentation and volume calculation. To make the segmentation algorithm work better, registration and partial volume effect algorithms were developed. The sensitivity of thresholding and the similarity index were calculated to verify the segmentation method. In order to test the volume calculation algorithm, an analytical phantom and physical phantoms with known volumes were used and percent error was calculated.

The range of the similarity index for our 15 clinical cases was 0.7 to 0.92 which was a good result. That shows that the segmentation method worked well. For the volume calculation method, the percent error of the ventricle volumes of the analytical phantom and the calculated ventricle volumes was in the range from 0.14% to 2.8%, which are very good results since 5% error rate was taken as acceptable [4][5][8]. The

percent error of the ventricle volume of the created model and the calculated ventricle volume varied from 0.23% to 5.2%. This also shows the volume calculation algorithm (CSV) gives results within an acceptable range.

When the patient has hydrocephalus, the ventricles become enlarged. By automatically calculating and comparing the volume of the ventricles at different times, our algorithm can aid in the diagnosis of hydrocephalus. In normal cases, the change in the calculated volume of the ventricle was less than 5%. In the clinical cases examined, when hydrocephalus was present, the change in the calculated volume of the ventricles was greater than 20%. Our algorithm was tested on eight clinical double cases. Therefore an CSV algorithm shows good potential as an aid in the diagnosis of hydrocephalus.

Chapter 7

Future Work

Some possible further work following from this thesis includes:

- The segmentation methods that we used are based on the gray values since the objects in brain have distinct gray values. However as Fig. 4.2d shows, the ventricles and surrounding tissue have distinct textures. Future work could include the investigation of segmentation based on texture.
- The idea of our algorithm is to do segmentation in 2D and then calculate the 3D volume. An alternative approach would be to create a model of the whole head in 3D from one set of slices, and then do segmentation and volume calculation in 3D.
- For the 3D interpolation, one kind of head displacement (head to shoulder) was corrected in this thesis. Another type of head displacement, the nod, was not addressed in this thesis since there were no easily identifiable features that could

be used as landmarks to calculate the tilt angle. This also is a potential topic for future work.

- The FOV was obtained from the DICOM header manually. In future developments this information could be automatically extracted from the header. Similarly the image formats were changed to allow easy manipulation. Future developments could use the DICOM image data directly.
- The thresholding and region growing algorithms depend on the manual selection of a region of interest. Future research could investigate method to select the region of interest without manual interruption.
- The eyeballs were used as landmarks for the interpolation algorithm. Future research could investigate methods, such as the Hough transform, to locate the eyeball centers and determine the eyeball size.

Bibliography

- [1] Agrawala, A.K., *Machine Pattern Recognition*, New York: IEEE Press, 1977.
- [2] Aggarwal, J.K., Duda, R.O., and Rosenfeld, A., *Computer Methods in Image Analysis*, New York: IEEE Press, 1977.
- [3] Ashburner, J., and Friston, K.J., "Voxel-Based Morphometry - The methods", The Wellcome Department of Cognitive Neurology, Institute of Neurology, Queen Square, London. Oct.1999.
- [4] Ashtari, M., Zito, J.L., Gold, B.I., Lieberman, J.A., Borenstein, M.T., Herman, P.G., "Computerized Volume Measurement of Brain Structure", *Investigative Radiology*, Vol. 25, 1990, pp.789-805.
- [5] Baldy, R.E., Brindley, G.S., Ewusi-Mensah, I., Jacobsen, R.R., Reveley, M.A., Turner, S.W., Lishman, W.A., "A Fully-Automated Computer-Assisted Method of CT Brain Scan Analysis for the Measurement of Cerebrospinal Fluid Spaces and Brain Absorption Density", *Neuroradiology*, Vol. 28, 1986, pp.109-117.
- [6] Bajcsy, R., and Kovacic, S., "Multiresolution Elastic Matching", *Comput. Vis., Graph.,Image Processing*, Vol. 46, Issue 1, 1989, pp.1-21.

- [7] Bookstein, F., "Principal Warp: Thin Plate Splines and the Decomposition of Deformations", IEEE Transaction on Pattern Anal. Machine Intell., Vol. 11, No. 6, June 1989, pp.567-585.
- [8] Brassow, F., Baumann, K., "Volume of Brain Ventricles in Man Determined by Computer Tomography", Neuroradiology, Vol. 16, 1978, pp.187-189.
- [9] Canny, J., "Computational Approach to Edge Detection", IEEE Trans. Pattern Analysis and Machine Intelligence, Vol. 8, No. 6, Nov. 1986, pp.679-698.
- [10] Choi, S.M., Lee, J.E., Kim, J., and Kim, M.H., "3D-MRF Model-Based Segmentation for Object Reconstruction of Medical Images", J.Korea Inform., Sci. Soc., A, Vol. 24, No. 7, 1997, pp.705-714.
- [11] Christensen, G., Rabbit, R., and Miller, M.I., "Deformable Templates Using Large Deformation Kinematics", IEEE Transaction on Medical Imaging, Vol. 5, No. 10, Oct. 1996, pp. 1435-1447.
- [12] Cohen, L., and Cohen, I., "Finite Element Method for Active Contour Models and Ballons for 2-D and 3-D Images", IEEE Transaction on Pattern Anal. Machine Intell., Vol. 15, Nov. 1993, pp. 1131-1147.
- [13] Collins, L. and Evans, A., "Animal: Validation and Applications of Nonlinear Registration-Based Segmentation", Int.J.Pattern Recogn. Artif. Intell., Vol. 8, No. 11, 1997, pp. 1271-1294.

- [14] Derin, H., and Elliot, H., "Modeling and Segmentation of Noisy and Textured Images Using Gibbs Random Fields", IEEE Transaction on Pattern Anal. Machine Intel., Vol. 9, Issue 1, Jan. 1987, pp.39-55.
- [15] Evans, J. "The Verification Of A Computer Algorithm Designed To Calculate The Volume Of The Human Cerebral Ventricles Based On CT Images", Psychology Honours thesis, Dalhousie Univ., submitted, May 2005.
- [16] Evans, J., "The Ice/Agar Phantom: The Development of A Dealistic Phantom Designed to Verify the Accuracy of A Computer Algorithm that Calculates the Volume of the Human Cerebral Ventricular System Based on CT Images", Technical Report Mathematics and Computing Science, St. Mary's Univ., Sep. 8, 2004.
- [17] Gemen, S., and Gemen, D., "Stochastic Relaxation, Gibbs Distribution, and the Bayesian Restoration of Images", IEEE Transaction on Pattern Anal. Machine Intell., Vol. PAMI-6, No. 6, 1984, pp. 721-741.
- [18] Gonzalez, R.C., and Woods, R.E., *Digital Image Processing*, Second edition, 2001, pp. 206-617.
- [19] Gregson, P.H., CVLAB software, Dalhousie University, 1996
- [20] Hipwell, J.H., Penney, G.P., Mclangulin, R.A., Rhode, K., Summers, P., Cox, T.C., " Intensity-Based 2-D-3-D Registration of Cerebral Angiograms", IEEE Transaction on Medical Imaging, Vol. 22, No. 11, Nov 2003.

- [21] Jie, Z., and Anand, R., "Affine Image Registration Using A New Information Metric", IEEE Computer Society Conference on Computer Vision and Pattern Recognition, Vol. 1, June 27- July 02, 2004, pp. 848-855.
- [22] Kak, A.C., Slaney, M., *Principles of Computerized Tomographic Imaging*, IEEE Press, New York, 1988, pp. 102-103.
- [23] Kelly, P.A., Derin, H., and Hartt, K.D., "Adaptive Segmentation of Speckled Images Using A Hierarchical Random Field Model", IEEE Trans. Acoust., Speech, Signal Processing, Vol. 36, Oct. 1988.
- [24] Kennedy, D.N., Filipek, P.A., Caviness, V.S., "Anatomic Segmentation and Volumetric Calculation in Nuclear Magnetic Resonance Imaging", IEEE Transaction on Medical Imaging, Vol. 8, No. 1, Aug 1997, pp. 1-7.
- [25] Koss, J.E., Newman, F., Johnson, T.K., Kirch, D.L., "Abdominal Organ Segmentation Using Texture Transforms and A Neural Network", IEEE Transaction on Medical Imaging, Vol. 18, No. 7, Jul 1999, pp. 640-648.
- [26] Kostis, W.J., Reeves, A.P., Yankelevitz, D.F., and Henschke, C.I., "Three- Dimensional Segmentation and Growth-Rate Estimation of Small Pulmonary Nodules in Helical CT Images", IEEE Transaction on Medical Imaging, Vol. 22, No. 10, Oct 2003.
- [27] Lakare, S., Wan, M., Sato, M., and Kaufman, A., "3D Digital Cleansing Using Segmentation Rays", Proceedings of the 11th IEEE Visualization 2000 Conference (VIS 2000), IEEE Computer Society, Oct. 2000.

- [28] Lakshmanan, S., and Derin, H., "Simultaneous Parameter Estimation and Segmentation of Gibbs Random Fields Using Simulated Annealing", IEEE Transaction on Pattern Anal. Machine Intell., Vol. PAMI-11, Issue. 8, 1989, pp. 799-813.
- [29] Liew, A.W, and Yan, H., "An Adaptive Spatial Fuzzy Clustering Algorithm for 3-D MR Image Segmentation", IEEE Transaction on Medical Imaging, Vol. 22, No. 9, Sep. 2003.
- [30] Livyatan, H., Yaniv, Z., and Joskowicz, L., "Gradient-Based 2-D/3-D Registration of Fluoroscopic X-Ray to CT, IEEE Transaction on Medical Imaging, Vol. 22, No. 11, Nov. 2003.
- [31] Muss, O., Heitz, F. and Armspach, J.P., "3-D Deformable Image Matching Using Multiscale Minimization of Global Energy Functions", in Proc.Conf. Computer Vision Pattern Recongition, Vol. 2, Fort Collins, CO, June 1999, pp. 478-485.
- [32] Muzic, R.F., Chen, C.H. and Nelson, A.D., "A Method to Correct for Scatter, Spillover, and Partical Volume Effects in Region of Interest Analysis in PET", IEEE Transaction on Medical Imaging, Vol. 17, No. 2, Apr 1998.
- [33] Nalwa, V.S., *A Guided Tour of Computer Vision*, Addison-Wesley Pub. Co., 1993.
- [34] Rohde, G.K., Aldroubi, A., Dawant, B.M., "The Adaptive Bases Algorithm for Intensity-Based Nonrigid Image Registration", IEEE Transaction on Medical Imaging, Vol. 22, No. 11, Nov 2003.

- [35] Rottenberg, D.A., Pentlow, K.S., Deck, M.D.F., Allen, J.C., “Determination of Ventricular Volume Following Metrizamide CT Ventriculography”, *Neuroradiology*, Vol. 16, 1978, pp. 136-139.
- [36] Schurr, P.H., Polkey, C.E., *Hydrocephalus*, Oxford Medical Publications, 1993, pp. 1.
- [37] Sonka, M., Hlavac, V., and Boyle, R., *Image Processing, Analysis, and Machine Vision*, second edition, 1999, pp. 123-130.
- [38] Shapiro, L.G., Stockman, G.C., *Computer Vision*, pp. 297-299.
- [39] Subsol, G., Thirion, J.P., and Anyache, N., “A General Scheme for Automatically Building 3-D Morphometric Anatomical Atlases: Application to A Skull Atlas”, *Med. Image Anal.* , Vol. 2, No. 1, 1998, pp. 37-60.
- [40] Sze, R.W., Ghioni, V., Weinberger, E., Seidel, K.D., Ellenbogen, R.G, “Rapid Computed Tomography Technique to Measure Ventricular Volumes in the Child with Suspected Ventriculoperitoneal Shunt Failure I; Validation of Technique with A Dynamic Phantom”, *Journal of Computer Assisted Tomography*, Vol. 27 (5), 2003a, pp. 663-667.
- [41] Szeliski, R., and Lavalley, S., “Matching 3-D Anatomical Surfaces with Nonrigid Deformation Using Octree-Aligners”, *SPIE Geometric Meth. Comput. Vis.*, Vol. 2031, 1993, pp. 306-315.

- [42] Westenberg, M.A., Roerdink, J.B.T.M., “Frequency Domain Volume Rendering by the Wavelet X-Ray Transform”, IEEE Transaction on Medical Imaging, Vol. 9, No. 7, Jul 2000, pp. 1249-1261.
- [43] Zhang, J., and Modestino, J.W., “Unsupervised Image Segmentation Using Gaussian Model”, in Proc. 22nd Annu. Conf. Inform. Sci. Syst., Princeton Univ., Princeton, NJ, Mar. 1988.
- [44] Zheng, Y., Nixon, M.S., and Allen, R., “Automated Segmentation of Lumbar Vertebrae in Digital Videofluoroscopic Images”, IEEE Transaction on Medical Imaging, Vol. 23, No. 1, Nov 2004.
- [45] <http://www.psychology.nottingham.ac.uk/staff/cr1/dicom.html>, Visited on Mar.1, 2005.
- [46] <http://biology.about.com/library/organs/brain/bllateralvent.htm>, Visited on Mar. 1, 2005.
- [47] <http://www.epub.org.br/cm/n02/fundamentos/ventriculos.i.htm>, Visited on Sep. 12, 2004.